Reza Mirzaeifar · Reginald DesRoches · Arash Yavari

Analysis of the Rate-Dependent Coupled Thermo-Mechanical Response of Shape Memory Alloy Bars and Wires in Tension

Abstract In this paper, the coupled thermo-mechanical response of shape memory alloy (SMA) bars and wires in tension is studied. By using the Gibbs free energy as the thermodynamic potential and choosing appropriate internal state variables, a three-dimensional phenomenological macroscopic constitutive model for polycrystalline SMAs is derived. Taking into account the effect of generated (absorbed) latent heat during the forward (inverse) martensitic phase transformation, the local form of the first law of thermodynamics is used to obtain the energy balance relation. The three-dimensional coupled relations for the energy balance in the presence of the internal heat flux and the constitutive equations are reduced to a one-dimensional problem. An explicit finite difference scheme is used to discretize the governing initial-boundary-value problem of bars and wires with circular cross sections in tension. Considering several case studies for SMA wires and bars with different diameters, the effect of loading-unloading rate and different boundary conditions imposed by free and forced convections at the surface are studied. It is shown that the accuracy of assuming adiabatic or isothermal conditions in the tensile response of SMA bars strongly depends on the size and the ambient condition in addition to the rate-dependency that has been known in the literature. The data of three experimental tests are used for validating the numerical results of the present formulation in predicting the stress-strain and temperature distribution for SMA bars and wires subjected to axial loading-unloading.

Keywords Shape memory alloy · Thermo-mechanical coupling · Rate-dependent response

1 Introduction

All the unique properties of shape memory alloys (SMAs) that have been the origin of extensive use of these materials in various applications are a result of SMAs inherent capability to have two stable lattice structures. The shape memory effect (SME) and the pseudoelastic response – two distinctive properties of SMAs – are both due to this ability of changing the crystallographic structure by a displacive phase transformation between the cubic austenite parent phase (the high symmetry phase preferred at high temperatures) and the low symmetry martensite phase (preferred at low temperatures) in response to mechanical and/or thermal loadings.

It has been observed that the response of an SMA single crystal is distinctly different from polycrystalline SMAs. There are micromechanical approaches for developing SMA constitutive relations for modeling the behavior of single crystals (Goo and Lexcellent, 1997; Gall *et al.*, 1999; Gao *et al.*, 2000). Using micromechanics for capturing the polycrystalline SMAs response can be seen in Patoor *et al.* (2006) and Lagoudas *et*

Reza Mirzaeifar
George W. Woodruff School of Mechanical Engineering, Georgia Institute of Technology, Atlanta, GA 30332, USA

Reginald DesRoches
School of Civil and Environmental Engineering, Georgia Institute of Technology, Atlanta, GA 30332, USA

Arash Yavari
School of Civil and Environmental Engineering, Georgia Institute of Technology, Atlanta, GA 30332, USA, E-mail: arash.yavari@ce.gatech.edu

al. (2006). A polycrystalline SMA consists of many grains with different crystallographic orientations. The phase transformation strongly depends on the crystallographic orientation and modeling the macroscopic response of SMAs by considering different phase transformation conditions in grains is extremely difficult. Considering the complexity of microstructure in polycrystalline SMAs one is forced to use macroscopic phenomenological constitutive equations for modeling the martensitic transformation. These models are based on continuum thermomechanics and construct a macroscopic free energy potential (Helmholtz or Gibbs free energy) depending on the state and internal variables used to describe the measure of phase transformation. Consequently, evolution equations are postulated for the internal variables and the second law of thermodynamics is used in order to find thermodynamic constraints on the material constitutive equations. In recent years, different constitutive models have been introduced by different choices of thermodynamic potentials, internal state variables, and their evolution equations. For a comprehensive list of one-dimensional and three-dimensional phenomenological SMA constitutive equations with different choices of thermodynamic potentials and internal state variables the reader is referred to Birman (1997), Lagoudas *et al.* (2006), and Lagoudas (2008). Besides different choices of potential energy and internal state variables, by considering the experimental results for the response of SMAs, various choices have been made for the hardening function. Among the most widely accepted models, we can mention the cosine model (Liang and Rogers, 1992), the exponential model (Tanaka *et al.*, 1995), and the polynomial model (Boyd and Lagoudas, 1996). Lagoudas *et al.* (1996) unified these models using a thermodynamic framework. In this paper, we use a phenomenological constitutive equation using the Gibbs free energy as the thermodynamic potential, the martensitic volume fraction and transformation strains as the internal state variables, and the hardening function in polynomial form.

The martensitic phase transformation in SMAs is associated with generation or absorption of latent heat in forward (austenite to martensite) and reverse (martensite to austenite) transformations. This has been shown in many experiments and the heat of transformation and the associate temperatures for the start and end of forward/reverse martensitic transformation can be determined by differential scanning calorimeter or DSC (Airoldi *et al.*, 1994; He and Rong, 2004; Liu and Huang, 2006). In the majority of the previous works in which loading is assumed quasi-static, it is assumed that material is exchanging the phase transformation-induced latent heat with the ambient such that the SMA device is always isothermal and in a temperature identical with the ambient during loading and unloading. We will show in this paper that the definition of quasi-static loading that guarantees an isothermal process is not absolute; it is affected by a number of parameters, e.g. the ambient condition and size of the structure. In other words, it will be shown that a very slow loading rate that can be considered a quasi-static loading for an SMA wire with a small diameter may be far from being quasi-static and isothermal for a bar with larger diameters. This size effect phenomenon has been reported previously in some experiments (DesRoches *et al.*, 2004; McCormick *et al.*, 2007), but we are not aware of any analytical or numerical analysis of this phenomenon in the literature. In some of the previously reported works in the literature, the effect of this latent heat and its coupling with mechanical response of SMAs was considered along with some simplifying assumptions.

In the literature, two extreme cases of isothermal and adiabatic processes are considered for quasi-static and dynamic loading conditions, respectively. Chen and Lagoudas (2000) considered impact-induced phase transformation and assumed adiabatic conditions for solving the problem of SMA rods subjected to an impact load. Lagoudas *et al.* (2003) considered the dynamic loading of polycrystalline shape memory alloy rods. They compared the effect of considering adiabatic and isothermal assumptions on the response of SMA bars subjected to axial loading. In some other works, more realistic heat transfer boundary conditions capable of modeling a heat exchange greater than zero (corresponding to the adiabatic process) and less than the maximum possible value (corresponding to an isothermal process) are considered. In these works, to simplify the coupled thermo-mechanical relations, it is assumed that the nonuniformity of temperature distribution is negligible. Auricchio *et al.* (2008) studied the rate-dependent response of SMA rods by taking the latent heat effect and the heat exchange with ambient into consideration. The authors used the fact that for a wire with a small diameter temperature in the cross section is distributed uniformly during loading and unloading. A simplified one-dimensional constitutive relation and an approximate heat convection coefficient were considered for obtaining the thermo-mechanical governing equations. In a similar work, Vitiello *et al.* (2005) used the one-dimensional Tanaka's model (Tanaka *et al.*, 1986; Tanaka, 1986) in conjunction with the energy balance equation to take into account the latent heat effect. The solution was restricted to very slender cylinders with small Biot numbers. In this special case, temperature nonuniformity in the cross section is neglected and the governing equations are simplified by assuming a uniform temperature distribution at each time increment. Messner and Werner (2003) studied the local increase of temperature near a moving phase transformation front due to the latent heat of phase transformation in one-dimensional

SMAs subjected to tensile loading. They modeled the effect of phase transformation latent heat by a moving heat source. A constant value is considered for the latent heat generated by phase transformation. This assumption is unrealistic for polycrystalline SMAs because the amount of generated heat is specified by a set of coupled equations and depends on many variables, e.g. stress and martensitic volume fraction. Iadicola and Shaw (2004) used a special plasticity-based constitutive model with an up-down-up flow rule within a finite element framework and investigated the trends of localized nucleation and propagation phenomena for a wide range of loading rates and ambient thermal conditions. The local self-heating due to latent heat of phase transformation and its effect on the number of nucleations and the number of transformation fronts were studied. The effect of ambient condition was also considered by assuming various convection coefficients.

Bernardini and Vestroni (2003) studied the non-linear dynamic response of a pseudoelastic oscillator embedded in a convective environment. In this work, a simplified one-dimensional equation is considered by assuming the whole pseudoelastic device in a uniform temperature at each time step and the dynamic response of pseudoelastic oscillator is studied. Chang *et al.* (2006) presented a thermo-mechanical model for a shape memory alloy (SMA) wire under uniaxial loading implemented in a finite element framework. They assumed the temperature distribution in the cross section of wire to be uniform but a nonuniform distribution is assumed along the SMA wire. It is assumed that the phase transformation initiates in a favorable point of the wire (this point is defined by a geometric imperfection or stress concentration). The phase transformation front moves along the wire with a specific finite velocity. They studied the movement of phase transformation front and the temperature change along the wire analytically and experimentally. In this paper, we will consider a three-dimensional phenomenological macroscopic constitutive relation in conjunction with the energy balance equation for deriving the coupled thermo-mechanical equations governing the SMAs considering the effect of latent heat and the heat flux in the material due to temperature nonuniformity caused by the generated heat during forward phase transformation and the absorbed heat during the reverse phase transformation. The constitutive relations can be used for calculating the continuum tangent moduli tensors for developing numerical formulations (Qidwai and Lagoudas, 2000b; Mirzaeifar *et al.*, 2009), but coupling these equations with the energy relation in the rate form is extremely difficult in numerical methods. An alternative method for analysis of SMAs is using analytic and semi-analytic solutions with an explicit form of the constitutive relations for a specific geometry and loading (Mirzaeifar *et al.*, 2010a,b, 2011). In this paper, for the special one-dimensional case, an explicit expression is given for the stress-strain relation and the coupled energy equation will be in a rate form. For deriving the one-dimensional governing equations, a nonuniform distribution is considered in the cross section for all the variables including the stress, temperature, transformation strain and martensitic volume fraction and it is assumed that the material does not contain a favorable point for the initiation of phase transformation along the length (all the parameters are independent of axial location). These equations are discretized for wires and bars with circular cross sections using an explicit finite difference method. The discretized form of convection boundary conditions is also derived. For modeling SMA wires and bars operating in still air and exposed to air or fluid flow with a known speed, free and forced convection coefficients are calculated for slender wires and thick cylindrical bars in air and fluid using the experimental and analytical formulas in the literature. The results of the present formulation are compared with some experiments to verify the capability of our approach in modeling the rate dependency and calculating accurate temperature changes during loading-unloading. Several case studies are presented for studying the loading rate and ambient effects on the coupled thermo-mechanical response of SMA wires and bars. It is shown that a load being quasi-static or dynamic strongly depends on the ambient conditions and the specimen size and the temperature distribution may be non-uniform in thick bars.

The present study introduces the effects of considering the heat flux in the cross section and the ambient condition on the coupled thermo-mechanical behavior of SMA bars and wires for the first time in the literature. The generation and absorption of heat during the forward and inverse phase transformation causes a temperature gradient that consequently leads to a non-uniform stress distribution in the cross section even for a uniform strain distribution. The difficulty of monitoring the temperature in the cross section experimentally, reveals the necessity of using the method of this paper for studying this phenomenon. It is shown in the numerical results that using the method of this paper for having an accurate temperature and stress distribution in the cross section and considering the ambient conditions into account explains the size effect in the response of SMA bars and wires that was reported previously in the experimental literature. Our method also gives a more precise description of quasi-static and dynamic loading for SMA bars and wires depending on the size effect and ambient conditions.

This paper is organized as follows. In §2 the three-dimensional coupled thermo-mechanical governing equations for SMAs are obtained. The reduced one-dimensional form of these equations and an explicit stress-strain relation for the uniaxial loading of SMAs is given in §3. In §4, the governing equations and

initial/boundary conditions are discretized using an explicit finite difference scheme for wires and bars with circular cross sections. The method of calculating free and forced convection coefficients for cylinders in air are given in §5. The method of calculating the free convection coefficient for both slender and thick cylinders are also explained. §6 contains several case studies and the results of three experiments for verification purpose. Conclusions are given in §7.

2 Coupled thermo-mechanical governing equations for SMAs

For deriving the coupled thermo-mechanical governing equations for SMAs we start from the first law of thermodynamics in local form

$$\rho \dot{u} = \boldsymbol{\sigma} : \dot{\boldsymbol{\epsilon}} - \operatorname{div} \boldsymbol{q} + \rho \hat{g}, \tag{1}$$

where ρ is mass density, u is the internal energy per unit mass, $\boldsymbol{\sigma}$ and $\boldsymbol{\epsilon}$ are the stress and strain tensors, respectively. The parameters $\boldsymbol{q}$ and $\hat{g}$ are the heat flux and internal heat generation. The dot symbol on a quantity ($\dot{}$) represents time derivative of the quantity. The dissipation inequality reads

$$\rho \dot{s} + \frac{1}{T} \operatorname{div} \boldsymbol{q} - \frac{\rho \hat{g}}{T} \geq 0, \tag{2}$$

where s is the entropy per unit mass. Substituting the Gibbs free energy

$$G = u - \frac{1}{\rho} \boldsymbol{\sigma} : \boldsymbol{\epsilon} - sT, \tag{3}$$

into the dissipation inequality, another form of the second law of thermodynamics is obtained as

$$-\rho \dot{G} - \dot{\boldsymbol{\sigma}} : \boldsymbol{\epsilon} - \rho s \dot{T} \geq 0. \tag{4}$$

Note that

$$\dot{G} = \frac{\partial G}{\partial \boldsymbol{\sigma}} : \dot{\boldsymbol{\sigma}} + \frac{\partial G}{\partial T} \dot{T} + \frac{\partial G}{\partial \boldsymbol{\chi}} : \dot{\boldsymbol{\chi}}, \tag{5}$$

where $\boldsymbol{\chi}$ is the set of internal state variables. Substituting (5) into (4) gives

$$-\left(\rho \frac{\partial G}{\partial \boldsymbol{\sigma}} + \boldsymbol{\epsilon}\right) : \dot{\boldsymbol{\sigma}} - \rho \left(\frac{\partial G}{\partial T} + s\right) \dot{T} - \rho \frac{\partial G}{\partial \boldsymbol{\chi}} : \dot{\boldsymbol{\chi}} \geq 0. \tag{6}$$

Assuming the existence of a thermodynamic process in which $\dot{\boldsymbol{\chi}} = 0$ and noting that (6) is valid for all $\dot{\boldsymbol{\sigma}}$ and $\dot{T}$ (Qidwai and Lagoudas, 2000a), the following constitutive equations are obtained

$$-\rho \frac{\partial G}{\partial \boldsymbol{\sigma}} = \boldsymbol{\epsilon}, \quad -\frac{\partial G}{\partial T} = s. \tag{7}$$

The constitutive relations (7) are valid everywhere at the boundary of the thermodynamic region as well (Rajagopal and Srinivasa, 1998). Substituting (7) into (6), the dissipation inequality is expressed in a reduced form as

$$-\rho \frac{\partial G}{\partial \boldsymbol{\chi}} : \dot{\boldsymbol{\chi}} \geq 0. \tag{8}$$

In the present study, we consider the transformation strain $\boldsymbol{\epsilon}^t$ and the martensitic volume fraction ξ as the internal state variables[1]. The Gibbs free energy G for polycrystalline SMAs is given by (Boyd and Lagoudas, 1996; Qidwai and Lagoudas, 2000a):

$$G(\boldsymbol{\sigma}, T, \boldsymbol{\epsilon}^t, \xi) = -\frac{1}{2\rho} \boldsymbol{\sigma} : \mathbb{S} : \boldsymbol{\sigma} - \frac{1}{\rho} \boldsymbol{\sigma} : \left[\boldsymbol{\alpha} \left(T - T_0\right) + \boldsymbol{\epsilon}^t\right] + c \left[\left(T - T_0\right) - T \ln\left(\frac{T}{T_0}\right)\right]$$

$$- s_0 T + u_0 + \frac{1}{\rho} f(\xi), \tag{9}$$

---

[1] The portion of strain that is recovered due to reverse phase transformation from detwinned martensite to austenite is considered as the transformation strain. See Patoor *et al.* (2006) for a detailed description of the transformation strain and martensitic volume fraction.

where, $\mathbb{S}, \boldsymbol{\alpha}, c, s_0$ and u_0 are the effective compliance tensor, effective thermal expansion coefficient tensor, effective specific heat, effective specific entropy, and effective specific internal energy at the reference state, respectively. The symbols $\boldsymbol{\sigma}$ and T_0 denote the Cauchy stress tensor and reference temperature. The other parameters and symbols are all given previously. The effective material properties in (9) are assumed to vary with the martensitic volume fraction (ξ) as

$$\mathbb{S} = \mathbb{S}^A + \xi \Delta \mathbb{S}, \quad \boldsymbol{\alpha} = \boldsymbol{\alpha}^A + \xi \Delta \boldsymbol{\alpha}, \quad c = c^A + \xi \Delta c, \quad s_0 = s_0^A + \xi \Delta s, \quad u_0 = u_0^A + \xi \Delta u_0, \tag{10}$$

where the superscripts A and M represent the austenite and martensite phases, respectively. The symbol $\Delta(.)$ denotes the difference of a quality (.) between the martensitic and austenitic phases, i.e. $\Delta(.) = (.)^M - (.)^A$. In (9), $f(\xi)$ is a hardening function that models the transformation strain hardening in the SMA material. In this study we use the Boyd-Lagoudas' polynomial hardening model that is given by

$$f(\xi) = \begin{cases} \frac{1}{2}\rho b^M \xi^2 + (\mu_1 + \mu_2)\,\xi, & \dot{\xi} > 0, \\ \frac{1}{2}\rho b^A \xi^2 + (\mu_1 - \mu_2)\,\xi, & \dot{\xi} < 0, \end{cases} \tag{11}$$

where, ρb^A, ρb^M, μ_1 and μ_2 are material constants for transformation strain hardening. The condition $(11)_1$ refers to the forward phase transformation ($A \to M$) and $(11)_2$ refers to the reverse phase transformation ($M \to A$).

Another form of the first law of thermodynamics is obtained by substituting (7) and (5) into (1) and considering the set of internal state variables as $\boldsymbol{\chi} = \{\boldsymbol{\epsilon}^t, \xi\}$. This form is given by

$$\rho T \dot{s} = \rho \frac{\partial G}{\partial \boldsymbol{\epsilon}^t} : \dot{\boldsymbol{\epsilon}}^t + \rho \frac{\partial G}{\partial \xi} \dot{\xi} - \mathrm{div}\boldsymbol{q} + \rho \hat{g}. \tag{12}$$

The constitutive relation $(7)_2$ is used for calculating the time derivative of the specific entropy as

$$\dot{s} = -\frac{\partial \dot{G}}{\partial T} = -\frac{\partial^2 G}{\partial \boldsymbol{\sigma} \partial T} : \dot{\boldsymbol{\sigma}} - \frac{\partial^2 G}{\partial T^2} \dot{T} - \frac{\partial^2 G}{\partial \boldsymbol{\epsilon}^t \partial T} : \dot{\boldsymbol{\epsilon}}^t - \frac{\partial^2 G}{\partial \xi \partial T} \dot{\xi}. \tag{13}$$

Substituting (9) into (13), the third term on the right hand side of (13) is zero and the rate of change of specific entropy is given by

$$\dot{s} = \frac{1}{\rho} \boldsymbol{\alpha} : \dot{\boldsymbol{\sigma}} + \frac{c}{T} \dot{T} + \left[\frac{1}{\rho} \Delta \boldsymbol{\alpha} : \boldsymbol{\sigma} - \Delta c \ln\left(\frac{T}{T_0}\right) + \Delta s_0 \right] \dot{\xi}. \tag{14}$$

Before substituting (14) into (12) for obtaining the final form of the first law, it is necessary to introduce a relation between the evolution of the selected internal state variables. By ignoring the martensitic variant reorientation effect, it can be assumed that any change in the state of the system is only possible by a change in the internal state variable ξ. The time derivative of the transformation strain tensor is related to the time derivative of the martensitic volume fraction as (Lagoudas, 2008)

$$\dot{\boldsymbol{\epsilon}}^t = \boldsymbol{\Gamma} \dot{\xi}, \tag{15}$$

where $\boldsymbol{\Gamma}$ represents a transformation tensor related to the deviatoric stress and determines the flow direction as

$$\boldsymbol{\Gamma} = \begin{cases} \frac{3}{2} H \frac{\boldsymbol{\sigma}'}{\bar{\sigma}}, & \dot{\xi} > 0, \\ H \frac{\boldsymbol{\epsilon}^{tr}}{\bar{\epsilon}^{tr}}, & \dot{\xi} < 0. \end{cases} \tag{16}$$

In (16), H is the maximum uniaxial transformation strain and $\boldsymbol{\epsilon}^{tr}$ represents the value of transformation strain at the reverse phase transformation. The terms $\boldsymbol{\sigma}'$, $\bar{\sigma}$ and $\bar{\epsilon}^{tr}$ are the deviatoric stress tensor, the second deviatoric stress invariant and the second deviatoric transformation strain invariant, respectively, and are expressed as: $\boldsymbol{\sigma}' = \boldsymbol{\sigma} - \frac{1}{3}(\mathrm{tr}\,\boldsymbol{\sigma})\mathbf{I}$, $\bar{\sigma} = \sqrt{\frac{3}{2}\boldsymbol{\sigma}' : \boldsymbol{\sigma}'}$, $\bar{\epsilon}^{tr} = \sqrt{\frac{2}{3}\boldsymbol{\epsilon}^{tr} : \boldsymbol{\epsilon}^{tr}}$, where $\mathbf{I}$ is the identity tensor. Substituting the flow rule (15) into the first term in the right hand side of (12) and considering the Gibbs free energy in (9), the thermodynamic force conjugated to the martenstic volume fraction is calculated as

$$\rho \frac{\partial G}{\partial \boldsymbol{\epsilon}^t} : \dot{\boldsymbol{\epsilon}}^t + \rho \frac{\partial G}{\partial \xi} \dot{\xi} = \left(-\boldsymbol{\sigma} : \boldsymbol{\Gamma} + \rho \frac{\partial G}{\partial \xi} \right) \dot{\xi} = -\pi \dot{\xi}, \tag{17}$$

where

$$\pi = \boldsymbol{\sigma} : \boldsymbol{\Gamma} + \frac{1}{2}\boldsymbol{\sigma} : \Delta\mathbb{S} : \boldsymbol{\sigma} + \Delta\boldsymbol{\alpha} : \boldsymbol{\sigma}\,(T - T_0\;) - \rho\Delta c \left[(T - T_0) - T \ln\left(\frac{T}{T_0}\right) \right]$$
$$+ \rho\Delta s_0 T - \frac{\partial f}{\partial \xi} - \rho\Delta u_0. \tag{18}$$

Introducing this new term (π) will remarkably simplify writing the constitutive and thermo-mechanical relations. Also, the second law of thermodynamics (8) can be written as $\pi\dot{\xi} \geq 0$. Substituting (17) and (14) into (12), the final form of the first law is obtained as

$$T\boldsymbol{\alpha} : \dot{\boldsymbol{\sigma}} + \rho c\dot{T} + \left[-\pi + T\Delta\boldsymbol{\alpha} : \boldsymbol{\sigma} - \rho\Delta c\,T \ln\left(\frac{T}{T_0}\right)\;+ \rho\Delta s_0 T \right]\dot{\xi} = -\mathrm{div}\boldsymbol{q} + \rho\hat{g}. \tag{19}$$

Let us now introduce the conditions that control the onset of forward and reverse phase transformations. Considering the dissipation inequality (8) as $\pi\dot{\xi} \geq 0$, a transformation function is introduced as

$$\Phi = \begin{cases} \pi - Y, & \dot{\xi} > 0, \\ -\pi - Y, & \dot{\xi} < 0, \end{cases} \tag{20}$$

where Y is a threshold value for the thermodynamic force during phase transformation. The transformation function represents the elastic domain in the stress-temperature space. In other words, when $\Phi < 0$ the material response is elastic and the martensitic volume fraction does not change ($\dot{\xi} = 0$). During the forward phase transformation from austenite to martensite ($\dot{\xi} > 0$) and the reverse phase transformation from martensite to austenite ($\dot{\xi} < 0$), the state of stress, temperature, and martensitic volume fraction should remain on the transformation surface, which is characterized by $\Phi = 0$. It can be seen that transformation surface in the stress-temperature space is represented by two separate surfaces that are defined by $\xi = 0$ and $\xi = 1$. Any state of stress-temperature inside the inner surface ($\xi = 0$) represents the austenite state with an elastic response. Outside the surface $\xi = 1$, the material is fully martensite and behaves elastically. For any state of stress-temperature on or in between these two surfaces the material behavior is inelastic and a forward transformation occurs. A similar transformation surface exists for the reverse phase transformation.

The consistency during phase transformation guaranteeing the stress and temperature states to remain on the transformation surface is given by (Simo and Hughes, 1998; Qidwai and Lagoudas, 2000a)

$$\dot{\Phi} = \frac{\partial\Phi}{\partial\boldsymbol{\sigma}} : \dot{\boldsymbol{\sigma}} + \frac{\partial\Phi}{\partial T}\dot{T} + \frac{\partial\Phi}{\partial\xi} : \dot{\xi} = 0. \tag{21}$$

Substituting (18) and (20) into (21) and rearranging gives the following expression for the martensitic volume fraction rate

$$\dot{\xi} = -\frac{(\boldsymbol{\Gamma} + \Delta\mathbb{S} : \boldsymbol{\sigma}) : \dot{\boldsymbol{\sigma}} + \rho\Delta s_0\dot{T}}{\mathscr{D}^{\pm}}, \tag{22}$$

where $\mathscr{D}^{+} = \rho\Delta s_0(M_s - M_f)$ for the forward phase transformation ($\dot{\xi} > 0$) and $\mathscr{D}^{-} = \rho\Delta s_0(A_s - A_f)$ for reverse phase transformation ($\dot{\xi} < 0$). The parameters A_s, A_f, M_s, M_f represent the austenite and martensite start and finish temperatures, respectively. Substituting (22) into (19) and assuming $\Delta\alpha = \Delta c = 0$ – valid for almost all practical SMA alloys – the following expression is obtained

$$[T\boldsymbol{\alpha} - \mathscr{F}_1(\boldsymbol{\sigma}, T)] : \dot{\boldsymbol{\sigma}} + [\rho c - \mathscr{F}_2(T)]\,\dot{T} = -\mathrm{div}\boldsymbol{q} + \rho\hat{g}, \tag{23}$$

where

$$\mathscr{F}_1(\boldsymbol{\sigma}, T) = \frac{1}{\mathscr{D}^{\pm}}(\boldsymbol{\Gamma} + \Delta\mathbb{S} : \boldsymbol{\sigma})(\mp Y + \rho\Delta s_0 T), \quad \mathscr{F}_2(T) = \frac{\rho\Delta s_0}{\mathscr{D}^{\pm}}(\mp Y + \rho\Delta s_0 T). \tag{24}$$

In (24) (+) is used for forward phase transformation and (-) is used for the reverse transformation. Equation (23) is one of the two coupled relations for describing the thermo-mechanical response of SMAs. The second relation is the constitutive equation obtained by substituting (9) into (7)$_1$ as

$$\boldsymbol{\epsilon} = \mathbb{S} : \boldsymbol{\sigma} + \boldsymbol{\alpha}\,(T - T_0) + \boldsymbol{\epsilon}^t. \tag{25}$$

3 Coupled thermo-mechanical relations in uniaxial tension

In this section we consider the uniaxial loading of a bar with circular cross section. Considering the cross section in the (r, θ)-plane and the bar axis along the z-axis, the only nonzero stress component is σ_z. Using $(16)_1$, the transformation tensor during loading (forward phase transformation) is written as

$$\boldsymbol{\Gamma}^+ = H \ \text{sgn}(\sigma_z) \begin{bmatrix} -0.5 & 0 & 0 \\ 0 & -0.5 & 0 \\ 0 & 0 & 1 \end{bmatrix}, \tag{26}$$

where sgn(.) is the sign function. Substituting (26) into (15) it is seen that if we denote the transformation strain along the bar axis by ϵ_z^t, the transformation strain components in the cross section are $\epsilon_r^t = \epsilon_\theta^t = -0.5\epsilon_z^t$ and the other components are zero during loading. This is equivalent to assuming that the phase transformation is an isochoric (constant-volume) process. Considering the same assumption (isochoric deformation due to phase transformation), the transformation tensor during reverse phase transformation is obtained as

$$\boldsymbol{\Gamma}^- = H \ \text{sgn}(\epsilon_z^{tr}) \begin{bmatrix} -0.5 & 0 & 0 \\ 0 & -0.5 & 0 \\ 0 & 0 & 1 \end{bmatrix}. \tag{27}$$

Substituting (27) into (18) and (20) and using the following relations between the constitutive model parameters:

$$\rho \Delta u_0 + \mu_1 = \frac{1}{2}\rho \Delta s_0 (M_s + A_f), \quad \rho b^A = -\rho \Delta s_0 (A_f - A_s),$$

$$\rho b^M = -\rho \Delta s_0 (M_s - M_f), \quad Y = -\frac{1}{2}\rho \Delta s_0 (A_f - M_s) - \mu_2, \tag{28}$$

$$\mu_2 = \frac{1}{4}(\rho b^A - \rho b^M), \quad \Delta \alpha = \Delta c = 0,$$

the following explicit expressions for the martensitic volume fractions in direct and inverse phase transformation in the case of uniaxial loading are obtained:

$$\xi^+ = \frac{1}{\rho b^M} \left\{ H|\sigma_z| + \frac{1}{2}\sigma_z^2 \Delta S_{33} + \rho \Delta s_0 (T - M_s) \right\}, \tag{29}$$

$$\xi^- = \frac{1}{\rho b^A} \left\{ H\sigma_z \ \text{sgn}(\epsilon_z^{tr}) + \frac{1}{2}\sigma_z^2 \Delta S_{33} + \rho \Delta s_0 (T - A_f) \right\}. \tag{30}$$

As the first step, we consider loading of a bar in tension ($\sigma_z \geq 0$). In this special case, substituting (26) into (15) and integrating the flow rule gives an explicit expression for transformation strain as $\epsilon_z^t = H\xi$, which after substitution into (25) gives the following one-dimensional constitutive equation

$$\epsilon_z = (S_{33}^A + \xi \Delta S_{33})\sigma_z + \alpha_A (T - T_0) + H\xi, \tag{31}$$

where $S_{33}^A = 1/E_A$, $\Delta S_{33} = 1/E_M - 1/E_A$ (E_A and E_M are the elastic muduli of austenite and martensite, respectively). Substituting the martensitic volume fraction (29) into (31), the stress-strain relation can be written as the following cubic equation

$$\sigma_z^3 + a \ \sigma_z^2 + (m \ T + n)\sigma_z + (p \ T + q) = 0, \tag{32}$$

where $a, m, n, p,$ and q are constants given by

$$a = \frac{3H}{\Delta S_{33}}, \quad m = \frac{2\rho \Delta s_0}{\Delta S_{33}}, \quad n = -\frac{2\rho \Delta s_0 M_s}{\Delta S_{33}} + \frac{2H^2 + 2\rho b^M S_{33}^A}{\Delta S_{33}^2},$$

$$p = \frac{2H\rho \Delta s_0 + 2\rho b^M \alpha_A}{\Delta S_{33}^2}, \quad q = \frac{-2H\rho \Delta s_0 M_s - 2\rho b^M (\alpha_A T_0 + \epsilon_z)}{\Delta S_{33}^2}. \tag{33}$$

The cubic equation (32) is solved for σ_z as a function of temperature and strain. The constitutive equation obtained from solving (32) is coupled with (23). The set of coupled thermo-mechanical equations to be solved in the uniaxial loading a bar with circular cross section is given by (the cross section is considered in

the (r, θ)-plane and the internal heat generation due to any source other than the phase transformation is ignored):

$$
\begin{cases}
\left[\alpha^A\, T - \tilde{\mathscr{F}}_1(\sigma_z, T) \right] \dot{\sigma}_z + \left[\rho c - \tilde{\mathscr{F}}_2(T) \right] \dot{T} = k \left(\frac{\partial^2 T}{\partial r^2} + \frac{1}{r} \frac{\partial T}{\partial r} \right), \\[2mm]
\sigma_z = \frac{1}{6}\mathscr{G}(T) - \frac{2mT + (2n - 2a^2/3)}{\mathscr{G}(T)} - \frac{a}{3},
\end{cases}
\tag{34}
$$

where

$$
\tilde{\mathscr{F}}_1(\sigma_z, T) = \frac{1}{\mathscr{D}^{\pm}}(H + \Delta S_{33}\sigma_z)(\mp Y + \rho \Delta s_0 T), \quad \tilde{\mathscr{F}}_2(T) = \frac{\rho \Delta s_0}{\mathscr{D}^{\pm}}(\mp Y + \rho \Delta s_0 T),
$$

$$
\mathscr{G}(T) = \left[f_1 T + f_0 + 12\sqrt{g_3 T^3 + g_2 T^2 + g_1 T + g_0} \right]^{1/3}.
\tag{35}
$$

The coefficients f_i and g_i are constants given by

$$
\begin{aligned}
& f_1 = 36ma - 108p, \;\; f_0 = 36na - 108q - 8a^3, \;\; g_3 = 12m^3, \;\; g_2 = -54amp - 3a^2m^2 + 36m^2n + 81p^2, \\
& g_1 = 12a^3 p - 54amq - 6a^2 mn + 36mn^2 + 162pq - 54anp, \\
& g_0 = 81q^2 + 12a^3 q + 12n^3 - 3a^2 n^2 - 54anq.
\end{aligned}
\tag{36}
$$

In $(34)_1$, k is the thermal conductivity and Fourier's law of thermal conduction ($\boldsymbol{q} = -k\boldsymbol{\nabla}T$) is used for deriving the right hand side.

As it is shown, both temperature and stress fields are functions of time and radius r. As initial conditions for (34) one prescribes stress and temperature distributions at $t = 0$:

$$
T(r, 0) = \hat{T}, \;\; \sigma_z(r, 0) = \hat{\sigma}_z.
\tag{37}
$$

As boundary conditions, temperature or heat convection on the outer surface can be given

$$
\text{Convection}: \;\; k\frac{\partial T(r, t)}{\partial r}\bigg|_{r=R} = h_\infty[T_\infty - T(R, t)]
\tag{38}
$$

$$
\text{Constant Temperature}: \;\; T(R, t) = T_1,
\tag{39}
$$

where h_∞ is the heat convection coefficient and T_∞ is the ambient temperature. R is the bar radius and T_1 is the constant temperature of the free surface. Another condition is obtained at the center of bar using the axi-symmetry of temperature distribution in the cross section as

$$
\frac{\partial T(r, t)}{\partial r}\bigg|_{r=0} = 0.
\tag{40}
$$

The coupled differential equations (34) with the initial and boundary conditions (37), (38), and (40) constitute the initial-boundary value problem governing an SMA bar (wire) in uniaxial tension.

4 Finite difference discretization of the thermo-mechanical governing equations

A finite difference method is used for solving the coupled thermo-mechanical governing equations (34) with boundary conditions given in (38) and (40), and the initial conditions (37). For discretizing (34) we use an explicit finite difference method because we are dealing with two coupled highly nonlinear equations; solving such equations is computationally very expensive using implicit schemes. The radius of the bar is divided into $M - 1$ equal segments of size Δr as shown in Figure 1.

The derivatives on the right hand side of $(34)_1$ are discretized using a central difference scheme as

$$
\begin{aligned}
\frac{\partial^2 T}{\partial r^2} + \frac{1}{r}\frac{\partial T}{\partial r} &= \frac{1}{r}\frac{\partial}{\partial r}\left(r\frac{\partial T}{\partial r} \right) \\
&= \frac{1}{r_i}\frac{(r\partial T\partial r)^n_{i+1/2} - (r\partial T\partial r)^n_{i-1/2}}{\Delta r} \\
&= \left(r_i + \frac{\Delta r}{2} \right)\frac{T^n_{i+1} - T^n_i}{r_i(\Delta r)^2} - \left(r_i - \frac{\Delta r}{2} \right)\frac{T^n_i - T^n_{i-1}}{r_i(\Delta r)^2},
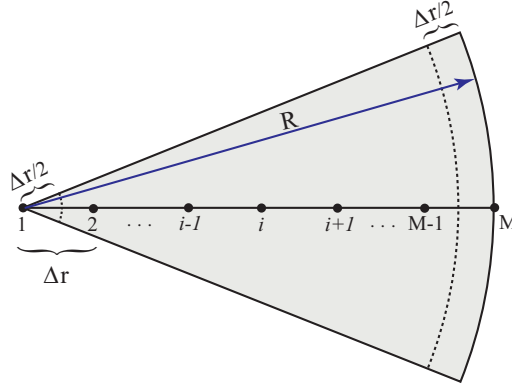\end{aligned}
\tag{41}
$$

Fig. 1 Internal and boundary nodes in the cross section for the finite difference discretization. The dashed lines are the boundaries of the control volumes attached to the central and boundary nodes used for deriving the finite difference form of the boundary conditions.

where the subscript i denotes the node number (see Figure 1) and the superscript n refers to the n*th* time increment. In explicit schemes, the first-order forward difference is used for approximating the time derivatives. The finite difference form of the coupled thermo-mechanical equations (34) using the explicit method is given by

$$\left[\alpha^A\, T_i^n - \frac{1}{\mathscr{D}^\pm}(H + \Delta S_{33}\sigma_{z,i}^n)(\mp Y + \rho\Delta s_0 T_i^n)\right]\frac{\sigma_{z,i}^{n+1} - \sigma_{z,i}^n}{\Delta t} + \left[\rho c - \frac{\rho\Delta s_0}{\mathscr{D}^\pm}(\mp Y + \rho\Delta s_0 T_i^n)\right]\frac{T_i^{n+1} - T_i^n}{\Delta t}$$
$$= \left(r_i + \frac{\Delta r}{2}\right)\frac{T_{i+1}^n - T_i^n}{r_i(\Delta r)^2} - \left(r_i - \frac{\Delta r}{2}\right)\frac{T_i^n - T_{i-1}^n}{r_i(\Delta r)^2}, \quad (42)$$

$$\sigma_{z,i}^{n+1} = \frac{1}{6}\mathscr{G}(T_i^{n+1}) - \frac{2mT_i^{n+1} + (2n - 2a^2/3)}{\mathscr{G}(T_i^{n+1})} - \frac{a}{3}, \quad (43)$$

where $\sigma_{z,i}^n$ is the axial stress in the i*th* node at the n*th* time increment. For calculating the finite difference approximation of the boundary conditions for our problem that includes internal heat generation, energy balance for a control volume[2] should be considered. For the central node $i = 1$, consider a control volume with radius $\Delta r/2$ as shown in Figure 1. The finite difference approximation of the boundary condition in the central node is given by (Özişik, 1994)

$$k\,\frac{T_2^n - T_1^n}{2} + \frac{1}{8}(\Delta r)^2\,\Re_1^n = \frac{1}{8}(\Delta r)^2\rho c\frac{T_1^{n+1} - T_1^n}{\Delta t}, \quad (44)$$

and for the outer node with the convection boundary condition, considering a control volume attached to the outer radius like that shown in Figure 1 with the dashed line, the energy balance gives

$$Rh_\infty(T_\infty - T_M^n) + k\left(R - \frac{\Delta r}{2}\right)\frac{T_{M-1}^n - T_M^n}{\Delta r} + \left[\frac{R\Delta r}{2} - \frac{(\Delta r)^2}{4}\right]\Re_M^n = \left[\frac{R\Delta r}{2} - \frac{(\Delta r)^2}{4}\right]\rho c\frac{T_M^{n+1} - T_M^n}{\Delta t}, \quad (45)$$

where the parameters $\Re_1^n$ and $\Re_M^n$ are the equivalent internal heat generation due to phase transformation calculated at the central ($i = 1$) and outer ($i = M$) nodes. For calculating the equivalent internal heat generation, consider the diffusion equation in cylindrical coordinates for a transient problem with internal heat generation $\hat{g}$ as (Arpaci, 1966)

$$k\left(\frac{\partial^2 T}{\partial r^2} + \frac{1}{r}\frac{\partial T}{\partial r}\right) + \hat{g} = \rho c\frac{\partial T}{\partial t}. \quad (46)$$

---

[2] To obtain the governing equations for the central and boundary nodes, a volume attached to these nodes (e.g. a region with width $\Delta r/2$ as shown in Figure 1) is considered and the energy balance is written for this control volume.

Comparing $(34)_1$ with (46), we define an equivalent internal heat generation corresponding to the ith node as

$$\Re_i^n = \left[\alpha^A \, T_i^n - \frac{1}{\mathscr{D}^\pm}(H + \Delta S_{33}\sigma_{z,i}^n)(\mp Y + \rho\Delta s_0 T_i^n) \right] \frac{\sigma_{z,i}^{n+1} - \sigma_{z,i}^n}{\Delta t} + \left[-\frac{\rho\Delta s_0}{\mathscr{D}^\pm}(\mp Y + \rho\Delta s_0 T_i^n) \right] \frac{T_i^{n+1} - T_i^n}{\Delta t},$$
$$(47)$$

where $\sigma_{z,i}^{n+1}$ is given in (43).

Considering the fact that at the nth loading increment stress and temperatures are known (these parameters are known from the initial condition (37) in the first time increment), for any of the nodes except the central and outer nodes, substituting (43) into (42) in the nth increment a nonlinear algebraic equation is obtained with only one unknown $T_i^{n+1}, i = 2...M - 1$. This equation is solved numerically (Forsythe *et al.*, 1976) and the temperature at the (n+1)th time increment is calculated. Substituting the calculated temperature into (43) gives the stress for (n+1)th increment. For the central and outer nodes, a similar procedure is used considering (43), (44), (45), and (47).

5 Convection boundary conditions

In most practical applications, SMA devices are surrounded by air during loading-unloading. In cases in which the device is working in conditions with negligible air flow, a free convection occurs around the device due to temperature changes caused by phase transformation. For all the outdoor structural applications of SMAs, the device is exposed to airflow and a forced convection boundary condition should be considered. For studying the effect of ambient on the thermo-mechanical response of SMAs, both free and forced convection boundary conditions are considered in this paper and the convection coefficient is calculated by considering a vertical[3] SMA bar or wire in still or flowing air with different velocities.

5.1 Free convection for SMA Bars in still air

When airflow speed is negligible, a free convection boundary condition should be considered around the SMA device. Considering an SMA vertical cylinder in still air, it is shown by Cebeci (1974) that the cylinder is thick enough to be considered a flat plate in calculating the convection coefficient with less than 5.5% error if $\mathsf{Gr}_L^{0.25} D/L \geq 35$, where $\mathsf{Gr}_x = g\beta(T_w - T_\infty)x^3/\upsilon^2$ is the Grashof number, $D = 2R$ is the cylinder diameter, g is the gravitational acceleration, β is the volume coefficient of expansion, i.e. $\beta = 1/T$ for ideal gasses, T_w is the wall temperature, T_∞ is the ambient temperature, υ is the kinematic viscosity of air, and x is a characteristic dimension, e.g. height or diameter of the cylinder. The Nusselt number for a flat plate with height L is given by (Holman, 1990; Popiel, 2008)

$$\mathsf{Nu}_{\mathrm{FP}} = 0.68 + \frac{0.67 \, \mathsf{Ra}_L^{0.25}}{[1 + (0.49 \, \mathsf{Pr})^{0.56}]^{0.44}}, \tag{48}$$

where $\mathsf{Ra}_L = \mathsf{Gr}_L\mathsf{Pr}$ is the Rayleigh number and Pr is the Prandtl number for air in the ambient temperature. Having the Nusselt number, the free convection coefficient for the cylinder is calculated by $\mathsf{Nu} = h_\infty x/k$, where x is the characteristic length (the height of cylinder in this case) and k is the air thermal conductivity at the ambient temperature. For studying slender cylinders with $\mathsf{Gr}_L^{0.25} D/L \leq 35$ or for avoiding the error in the case of considering thick cylinders, the following correction can be used (Popiel, 2008)

$$\frac{\mathsf{Nu}_c}{\mathsf{Nu}_{\mathrm{FP}}} = 1 + 0.30 \left[\sqrt{32} \, \mathsf{Gr}_L^{-0.25} \left(\frac{L}{D} \right) \right]^{0.91}. \tag{49}$$

The free convection coefficient around the cylinder is calculated by substituting (48) into (49) and using $\mathsf{Nu}_c = h_\infty L/k$.

---

[3] In forced convection, a vertical bar is perpendicular to the air flow. In free convection, the gravitational acceleration is parallel to the axis of a vertical bar.

Table 1 SMA material parameters

Material constants	Material I, Auricchio et al. (2008)	Material II, Mc-Cormick et al. (2007)	Material III, DesRoches et al. (2004)	A generic SMA (Material IV), Lagoudas (2008)
E^A	$31.0 \times 10^9 \mathrm{Pa}$	$34.0 \times 10^9 \mathrm{Pa}$	$34.0 \times 10^9 \mathrm{Pa}$	$55.0 \times 10^9 \mathrm{Pa}$
E^M	$24.6 \times 10^9 \mathrm{Pa}$	$31.0 \times 10^9 \mathrm{Pa}$	$31.0 \times 10^9 \mathrm{Pa}$	$46.0 \times 10^9 \mathrm{Pa}$
$\nu^A = \nu^M$	0.3	0.33	0.33	0.33
α^A	$22.0 \times 10^{-6}/\mathrm{K}$	$22.0 \times 10^{-6}/\mathrm{K}$	$22.0 \times 10^{-6}/\mathrm{K}$	$22.0 \times 10^{-6}/\mathrm{K}$
α^M	$22.0 \times 10^{-6}/\mathrm{K}$	$22.0 \times 10^{-6}/\mathrm{K}$	$22.0 \times 10^{-6}/\mathrm{K}$	$22.0 \times 10^{-6}/\mathrm{K}$
ρc^A	3.9×10^6 J/(m³K)	5.8×10^6 J/(m³K)	5.8×10^6 J/(m³K)	2.6×10^6 J/(m³K)
ρc^M	3.9×10^6 J/(m³K)	5.8×10^6 J/(m³K)	5.8×10^6 J/(m³K)	2.6×10^6 J/(m³K)
k	18W/(mK)	18W/(mK)	18W/(mK)	18W/(mK)
H	0.041	0.036	0.038	0.056
$\rho \Delta s_0$	-0.52×10^6J/(m³K)	-0.16×10^6J/(m³K)	-0.29×10^6J/(m³K)	-0.41×10^6J/(m³K)
A_f	291.0 K	257.8 K	270.0 K	280.0 K
A_s	276.0 K	239.1 K	263.0 K	270.0 K
M_s	265.0 K	233.1 K	253.1 K	245.0 K
M_f	250.0 K	216.1 K	245.1 K	230.0 K

5.2 Forced convection for SMAs in air and fluid flow

For calculating the average convection heat transfer coefficients for the flowing air across a cylinder, the experimental results presented by Hilpert (1933) are used. The Nusselt number in this case can be calculated by (Holman, 1990)

$$\mathsf{Nu} = C \ \mathsf{Re}^n \ \mathsf{Pr}^{0.33}, \tag{50}$$

where $\mathsf{Re} = u_\infty D/\upsilon$ is Reynolds number and u_∞ is the airflow speed. The parameters C and n are tabulated in heat transfer books for different Reynolds numbers (e.g. see Chapter 6, Holman (1990)). Note that the characteristic length in Nusselt number for this case is the cylinder diameter and forced convection coefficient is calculated using $\mathsf{Nu} = h_\infty D/k$. Experimental results presented by Knudsen and Katz (1958) shows that (50) can be used for cylinders in fluids too. However, Fand (1965) has shown that for fluid flow on cylinders, when $10^{-1} < \mathsf{Re} < 10^5$, the following relation gives a more accurate Nusselt number

$$\mathsf{Nu} = (0.35 + 0.56 \ \mathsf{Re}^{0.52})\mathsf{Pr}^{0.3}. \tag{51}$$

6 Numerical results

6.1 Verification using experimental results

In order to verify our formulation for simulating the rate-dependent response of SMA bars and wires in simple tension, the experimental data previously reported by the second author (Auricchio et al., 2008) is used. The experiments were carried out using a commercial NiTi wire with circular cross section of radius $R = 0.5mm$. Since the alloy composition was unknown, simple tension tests were performed (Auricchio et al., 2008) and some basic material properties including the elastic moduli of austenite and martensite, the maximum transformation strain and the stress levels at the start and end of phase transformation process during loading and unloading were reported. These reported properties and the experimental results are used for calibrating the constants needed in the present constitutive equations. The material properties suitable for the constitutive relations of the present study are given in Table 1 as Material I.

In the experiments two different loading-unloading rates were considered. In the quasi-static test the total loading-unloading time is set to $\tau = 1000$ sec and the dynamic test was performed in $\tau = 1$ sec. Both tests were performed in the ambient temperature $T_\infty = 293K$. The experimental results for these two tests are depicted in Figure 3. In order to calculate the free convection coefficient, the method of §5.1 for slender cylinders is used. The length of the wire is $L = 20cm$ and the properties of air at $T = 293K$ are extracted from standard tables (Holman, 1990). The free convection coefficient is a function of the temperature difference between the wire and ambient $T_w - T_\infty$. Since T_w is unknown, it is difficult to satisfy the exact free convection boundary condition. But as it is depicted in Figure 2 (Case I), the free convection coefficient is almost constant for the range of temperature difference $0 < T_w - T_\infty < 40$. We will show in the

sequel that this temperature difference range matches the maximum temperature difference that is observed in an adiabatic loading-unloading for a vast range of SMA bar geometries, material properties, and ambient conditions. Therefore, an average value of $h_{\infty} = 21\ W/m^2K$ is considered during the loading-unloading process in this case. In the following case studies a similar analysis will be carried out for finding an average free convection coefficient.
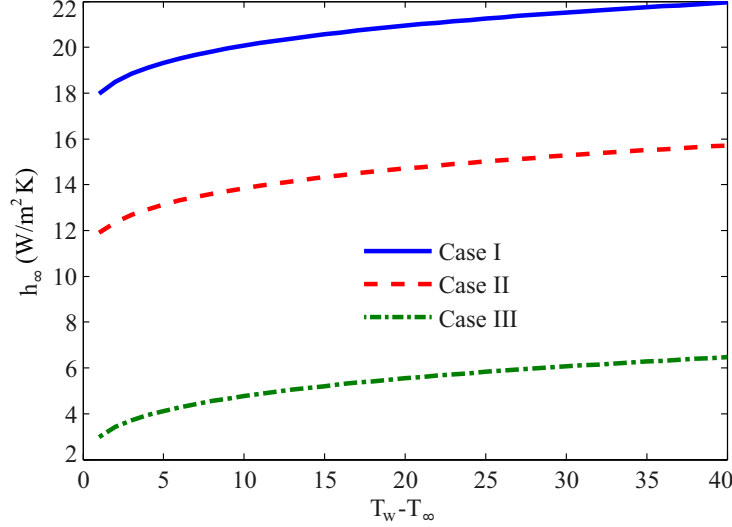

Fig. 2 The free convection coefficient as a function of temperature difference calculated for a vertical SMA cylinder with (Case I): $d = 1mm$, $L = 20cm$ in still air with $T = 293K$, (Case II): $d = 2mm$, $L = 10cm$ in still air with $T = 328K$, and (Case III): $d = 5cm$, $L = 10cm$ in still air with $T = 328K$.

The stress-strain response for quasi static and dynamic loading-unloading obtained by the present coupled thermo-mechanical formulation is compared with the experimental results in Figure 3. As it is seen, the analytical formulation predicts both the change of slope and change of hysteretic area in different loading-unloading rates. It is worth noting that the experimental loading-unloading curves in Figure 3 are stabilized cycles after a few initial cycles and a minor accumulated strain is observed at the beginning of loading that is ignored in the analytic results. In these experiments, the SMA temperature was not monitored. We will present a detailed study of the effect of ambient conditions and SMA bar geometry on the thermo-mechanical response of SMA bars with circular cross sections in uniaxial loading in the sequel. However, in order to validate the present formulation for simulating the thermo-mechanical response of SMAs, another experimental test is considered in this section.

The next experiment was performed by the second author on an SMA bar and the stress-strain response is reported in McCormick *et al.* (2007). In addition to the mechanical response, a pyrometer was used for monitoring the surface temperature of the SMA bar during loading-unloading. The specimen is made from a solid stock with a 12.7mm diameter. The specimen is subjected to a loading protocol with 20 cycles to 6% strain using a 250 kN hydraulic uniaxial testing apparatus. During the initial loading-unloading cycles accumulated strain is observed but for the last five cycles the material stress-strain response is stabilized. Here we consider the 20*th* stabilized loading-unloading cycle by setting the strain at the beginning of this cycle to zero (an accumulated strain of $\epsilon = 0.0057$ is observed at the beginning of the last cycle). Some of the material properties of the NiTi alloy for this bar are presented in (Tyber *et al.*, 2007) and the remaining parameters are calibrated using the stress and strain values corresponding to start and completion of phase transformation in the stress-strain response of the bar in uniaxial loading-unloading.

These material properties are given in Table 1 as Material II. The initial temperature of the bar at the beginning of the last cycle is $\hat{T} = 304.6K$ and the ambient temperature is $T_{\infty} = 301K$. The average free convection coefficient for the bar in this test is obtained using the method of the previous example and it is calculated as $h_{\infty} = 7.5\ W/m^2K$. The total loading-unloading time is $\tau = 114$ sec. The calculated temperature
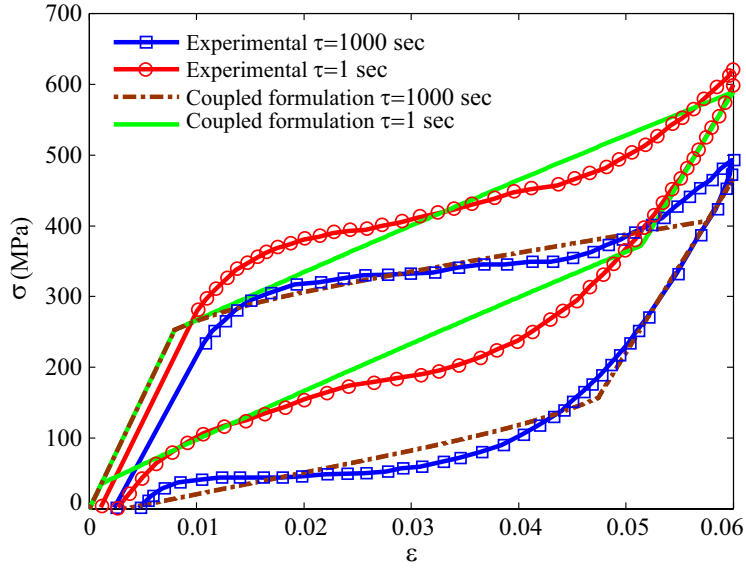
Fig. 3 Comparison of the experimental and analytical results for the stress-strain response of an SMA wire (Material I) with $d = 1mm$ in quasi-static and dynamic loadings (τ is the total loading-unloading time).

at the surface of the bar using the present formulation is compared with the experimental results in Figure 4(a). The experimental stress-strain response for the stabilized cycle is compared with the analytical results in 4(b). It is worth noting that the monitored temperature in the experimental data fluctuates and the smooth function in Matlab that uses a moving average filter is used to smoothen the data. As it is seen, the present formulation predicts the thermo-mechanical response of the bar with an acceptable accuracy.
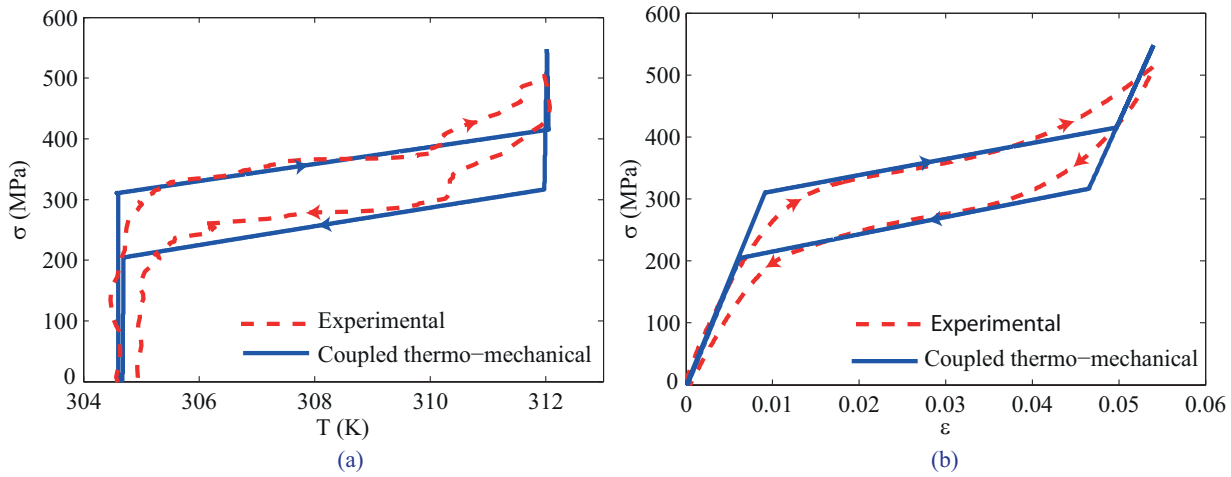
Fig. 4 Comparison of the experimental and analytical results for (a) stress-temperature at the surface, and (b) the stress-strain response of an SMA bar (Material II) with $d = 12.7mm$ in quasi-static loading-unloading ($\tau = 114$ sec).

As another case study, the experimental results of the cyclic loading of an SMA bar with 7.1mm diameter is considered. The experiment was performed by the second author and the stress-strain response of the bar in this test is reported in DesRoches *et al.* (2004). In this section we are considering the monitored surface

temperature of the bar in addition to the stress-strain response. This bar is made of NiTi alloy with the material properties given in Table 1 as Material III (some of these properties are given by the material provider and the others are calibrated using the uniaxial test results). The initial temperature of the bar and the ambient temperature are $\hat{T} = T_\infty = 298$K. The average free convection coefficient for the bar in this test is obtained using the method of the previous example and it is calculated as $h_\infty = 8 \ W/m^2 K$. The SMA bar is subjected to a dynamic cyclic loading consisting of 0.50%, 1.0-5% by increments of 1%, followed by four cycles at 6%. Frequency of the applied cyclic loading is 0.5Hz (2sec for each loading-unloading cycle). The stress-strain response of the bar obtained by the present coupled thermo-mechanical formulation is compared with the experimental results in Figure 5(a). It is seen that the analytical formulation predicts a slight upward movement of the hysteresis loop in the stress-strain response in each cycle. This phenomenon is also seen in the experimental results and is caused by the temperature increase during the fast loading-unloading cycles.
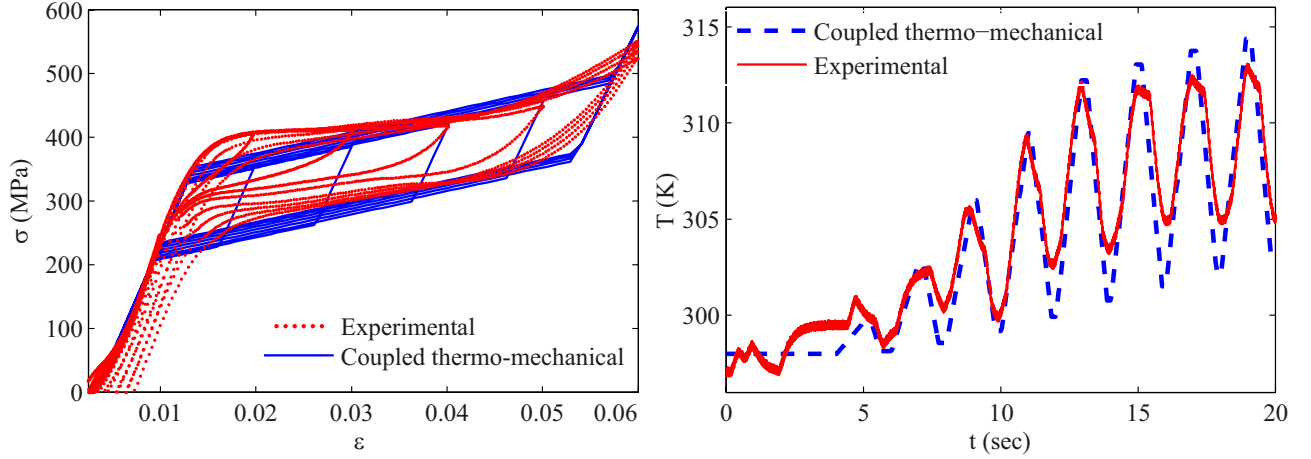

Fig. 5 Comparison of the experimental and analytical results for (a) the stress-strain response, and (b) temperature-time at the surface of an SMA bar (Material III) with $d = 7.1mm$ in dynamic cyclic loading.

The experimentally monitored temperature at the surface of bar is shown in Figure 5(b) and compared with the analytical results. It is seen that the analytical results are following the cyclic temperature change of the material with an acceptable accuracy (the maximum error in the analytical results is 1.15%). Both the experimental and analytical results show an increase of temperature at the start of each loading-unloading cycle with respect to its previous cycle. This temperature increase is the reason for the upward movement of the stress-strain hysteresis loops in Figure 5(a). It is worth noting that the experimental results show an accumulation in the strain for cyclic loading, typically referred to as the fatigue effect. Developing constitutive relations capable of modeling this accumulated cyclic strain accurately is an active field of research (Saint-Sulpice *et al.*, 2009; Paradis *et al.*, 2009). The present formulation is ignoring this effect. However, it is known that the constitutive equations used in this paper can be modified for accurate modeling of SMAs in cyclic loadings (Lagoudas and Entchev, 2004). Modifying the present coupled thermo-mechanical formulation for taking into account the effect of accumulated strains in cyclic loading will be the subject of a future communication.

6.2 SMA wires with convection boundary condition

In this section we consider some numerical examples for studying the effect of the loading-unloading rate and ambient conditions on the response of SMA wires in uniaxial tension based on our coupled thermo-mechanical formulation. An SMA wire with circular cross section of radius $R = 1mm$ and length $L = 10cm$ is considered. A generic SMA material with properties given in Table 1 as Material IV is considered (Lagoudas, 2008). These material properties have been used in many numerical simulations of SMAs. An approximate solution for the adiabatic and isothermal response of an SMA wire with these properties by ignoring the nonuniformity

of temperature distribution in the cross section and ambient conditions is presented in (Lagoudas, 2008). For comparison purposes, the initial temperature of the wire is considered equal to the value in Lagoudas (2008), i.e. $\hat{T} = 328K$. The ambient temperature is assumed to be $T_\infty = 328K$. The method of §5.1 is used for calculating the free convection coefficient as a function of temperature difference in the range $0 < T_w - T_\infty < 40$. The change of free convection coefficient versus the temperature change is plotted in Figure 2 (Case II). As it is seen, the convection coefficient does not change much with the temperature difference; assuming a constant value $h_\infty = 14.04 \, W/m^2K$ is a good approximation. The response of this SMA wire subjected to free convection in three different loading rates is modeled based on the present coupled thermo-mechanical formulation. Figure 6(a) shows the temperature changes during loading-unloading for three different rates in free convection. The stress-strain response in this case is shown in Figure 6(b). As the cross section diameter is small compared to its length, a uniform temperature distribution is observed in the cross section. Comparing these with those of the adiabatic solution by ignoring the ambient condition in Lagoudas (2008), it is seen that the response of the SMA wire in total loading-unloading time of $\tau = 10sec$ and exposed to a free convection boundary condition is identical with the adiabatic case. This is expected as the convection coefficient is low and loading is applied fast and hence the material cannot exchange heat with the ambient. For the loading-unloading times of $\tau = 120$ and $900sec$, as it is shown in Figure 6(a), although the temperature changes are less than that of $\tau = 10sec$, they cannot be ignored, i.e. assuming an isothermal process is not justified. As it is seen, for slow loading-unloading ($\tau = 120$ and $900sec$), the temperature increase during the forward phase transformation is suppressed. After phase transformation completion, and also during the initial elastic unloading regime, when there is no phase transformation heat generation or absorption, the air cooling effect causes a decrease in temperature. This temperature decrease when accompanied by heat absorption during the reverse phase transformation, causes the material to be colder than the initial and ambient temperatures at the end of the unloading phase.
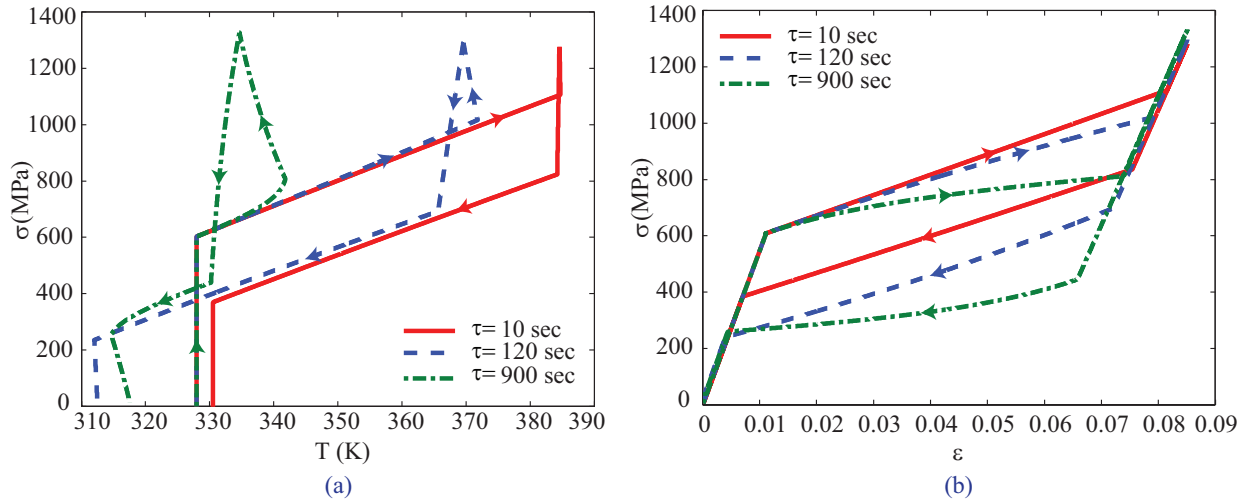

Fig. 6 The effect of total loading-unloading time τ on (a) stress-temperature, and (b) stress-strain response of an SMA wire with $d = 2mm$ in free convection (still air with $h_\infty = 14.04W/m^2K$).

The effect of ambient boundary condition on the response of SMA wires is studied in Figure 7. For this purpose a constant loading-unloading time of $\tau = 60sec$ and different air flow speeds are considered. The method of §5.2 is used for calculating the forced convection coefficients for $U_\infty = 15$ and $50m/s$ and these values are obtained as $h_\infty = 269.05$ and $493.20W/m^2K$, respectively. The free convection coefficient is the same as that of the previous example. Figure 7(a) shows the change of temperature versus stress for various air flow speeds and the stress-strain response of SMA wires is shown in Figure 7(b). As it is seen, temperature is strongly affected by the ambient condition. The temperature at the end of unloading phase is lower than the ambient and initial temperatures. During loading, after the phase transformation completion, and also at the beginning of unloading, before the start of reverse phase transformation, the material is
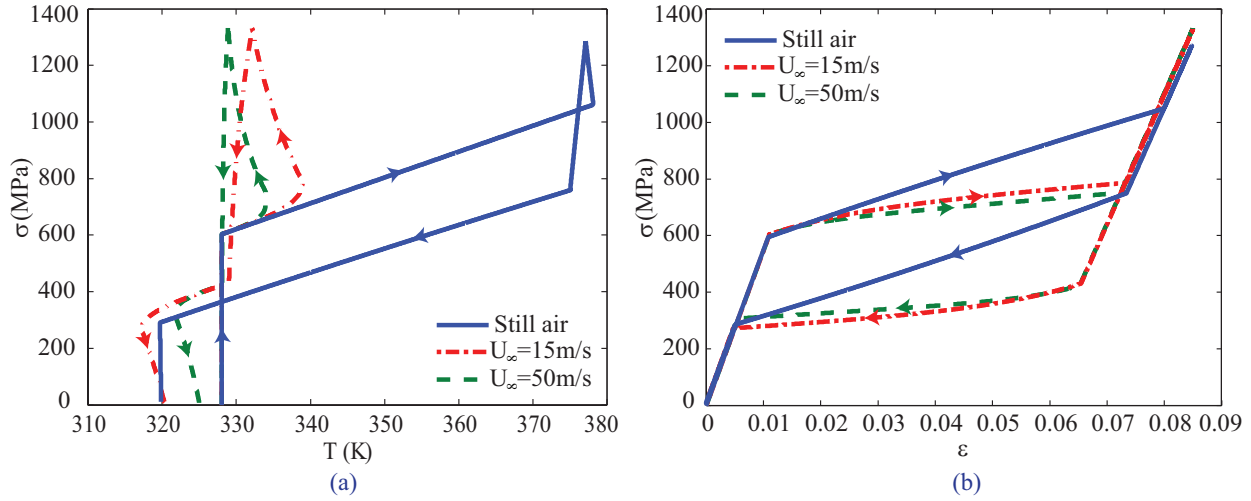
Fig. 7 The effect of airflow speed U_∞ on (a) stress-temperature, and (b) stress-strain response of an SMA wire with $d = 2mm$ in free and forced convection (the total loading-unloading time is $\tau = 60$sec).

fully martensite and phase transformation does not occur. During these steps, the transformation heat is not generating and the material is cooling due to the high rate of heat exchange with the ambient. This temperature loss is followed by heat absorption during reverse phase transformation and causes the material to be colder than the initial and ambient temperatures at the end of unloading phase. As shown in Figure 7(b), temperature change affects the stress-strain response as well. By increasing the air flow speed, when the material response changes from adiabatic to isothermal, the slope of stress-strain curve decreases and the hysteresis area increases. As mentioned earlier, this change in the hysteresis area, caused by a change in temperature during loading-unloading has been observed in experiments (see §6.1, McCormick *et al.* (2007) and Auricchio *et al.* (2008)).

6.3 SMA bars with convection boundary condition

In the previous section the response of SMA wires with small cross section diameters was studied. In this section SMA bars will be considered. In bars, in contrast with wires, the temperature distribution in the cross section is not uniform. It will be shown that for having a precise description of an SMA bar response in loading-unloading it is necessary to consider the coupled thermo-mechanical equations and the ambient conditions; assuming an isothermal response may cause considerable errors. An SMA bar with the material properties identical with those in the previous section is considered. The bar has a diameter of $d = 5$cm and length of $L = 20$cm. Using the method of §5.1, the free convection coefficient as a function of the temperature difference is calculated and plotted in Figure 2 as Case III. Similar to previous examples, it is seen that the free convection coefficient is almost constant and assuming an average value of $h_\infty = 5.86W/m^2K$ is reasonable. The effect of the loading-unloading rate on the response of SMA bars is shown in Figure 8.

As it will be shown in the sequel, temperature has a nonuniform distribution in the cross section. Temperature at the center of the bar is plotted versus stress for various total loading-unloading times in Figure 8(a). It is seen that the results for $\tau = 10$sec are similar to those presented by Lagoudas (2008) which are obtained assuming adiabatic loading-unloading and ignoring the ambient condition and non-uniform temperature distribution in the cross section. It can be concluded that the response of the material is almost adiabatic for this fast loading rate. However, as it is seen in Figure 8(a), even for the total loading-unloading time of $\tau = 7200$sec, which is considered a quasi-static loading with isothermal response in the majority of the previously reported works, the temperature in the SMA bar of this example is far from that in either an isothermal or an adiabatic process. Also the final cooling as explained in the case of SMA wires is seen in slow loading-unloading rates. This example reveals the necessity of using a coupled thermo-mechanical formulation, especially for SMA bars with large diameters.
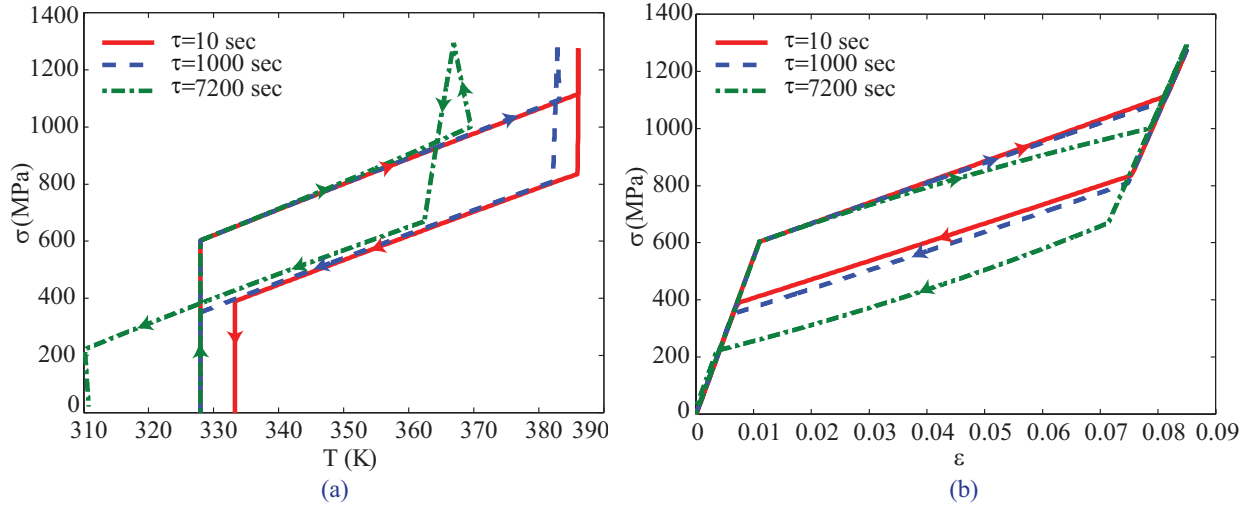
Fig. 8 The effect of total loading-unloading time τ on (a) stress-temperature, and (b) stress-strain response at the center of an SMA bar with $d = 5cm$ in free convection (still air with $h_\infty = 5.86W/m^2K$).

The stress-strain response at the center of the bar is shown in Figure 8(b). As it is seen in this figure, increasing the loading-unloading time decreases the stress-strain curve slope during the transformation and increases the hysteresis area. Comparing Figures 8 and 6 shows that increase of loading-unloading time affects the response of SMA wires more noticeably. This is expected because a wire has more potential for exchanging heat with the ambient air compared to a bar. The effect of air flow speed on the response of SMA bars in a constant loading-unloading time of $\tau = 300sec$ is shown in Figure 9. The forced convection coefficients are calculated using the method of §5.2 as $h_\infty = 134.37$ and $234.79W/m^2K$ for $U_\infty = 50$ and 100m/s, respectively. Temperature at the center of the bar versus stress is shown in Figure 9(a). As it is seen, even for the high air flow speed of $U_\infty = 100$m/s, the response of the SMA bar is not isothermal. Similar to SMA wires, cooling of material after completion of phase transformation and at the beginning of unloading causes the material to be in a lower temperature at the end of unloading compared to the initial temperature. The stress-strain response at the center of the bar for various air flow speeds is shown in Figure 9(b).

As mentioned earlier, for bars with large diameters, the temperature distribution in the cross section is not uniform because the heat transfer in regions near the surface differs from that in the central part. This non-uniformity in temperature distribution can be ignored for wires with small diameters but it is of more importance in bars with large diameters. Temperature distribution for the bar with $d = 5cm$ diameter subjected to free and forced convection at the end of loading phase is shown in Figure 10. As it is seen, for the total loading-unloading time of $\tau = 300$sec, the temperature distribution is almost uniform for the free convection case and becomes non-uniform when the bar is subjected to air flow. In all the cases, temperature at the center of the bar is maximum. Increasing the air flow speed decreases temperature at every point of the cross section. Temperature non-uniformity increases for higher airflow speeds. It is worth emphasizing that in the free convection case and for very slow loading-unloading rates a non-uniform temperature distribution is seen for SMA bars with large diameters.

6.4 Non-uniform stress distribution in uniaxial tension of an SMA bar

As mentioned earlier, the generation (absorption) of latent heat during forward (reverse) phase transformation and the heat exchange with the ambient at the surface of bars causes a nonuniform temperature distribution in the cross section. The non-uniformity of temperature increases for larger diameters, slower loading-unloading rates, and larger convection coefficients. Non-uniformity of temperature distribution is determined by the interaction of size, loading rate, and ambient conditions. Because of the strong coupling between the thermal and mechanical fields in SMAs temperature difference in the cross section causes a
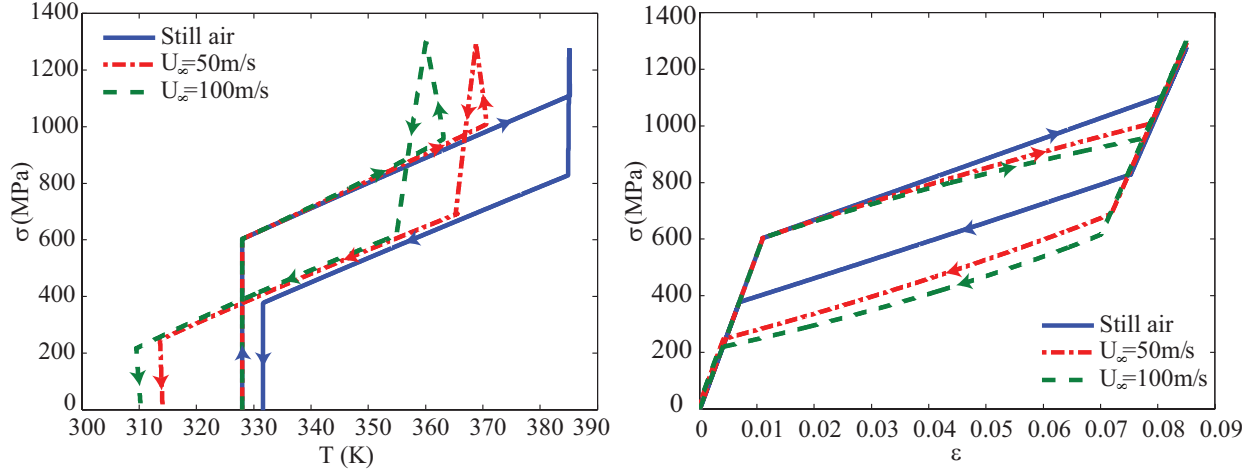
Fig. 9 The effect of airflow speed U_∞ on (a) stress-temperature, and (b) stress-strain response in the center of an SMA bar with $d = 5cm$ in free and forced convection (the total loading-unloading time is $\tau = 300sec$).
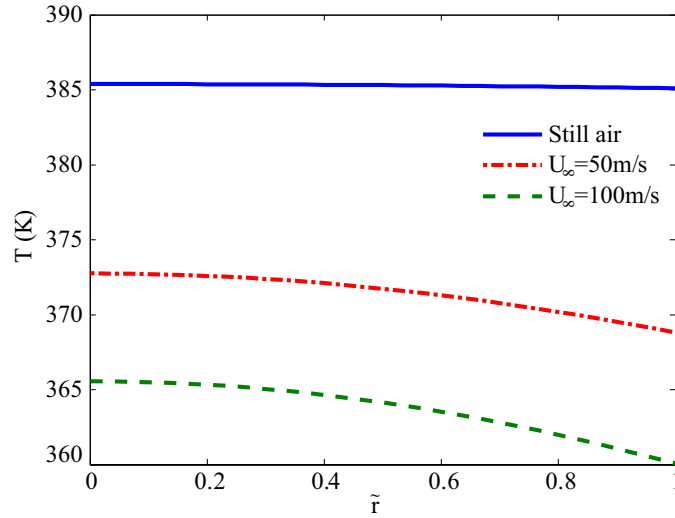

Fig. 10 The effect of airflow speed U_∞ on the temperature distribution in the cross section of an SMA bar with $d = 5cm$ in forced convection. The total loading-unloading time is $\tau = 300sec$ and the distribution is shown at the end of loading phase.

non-uniform stress distribution in the cross section. In other words, for uniaxial loading of an SMA bar, while the material in the cross section has a uniform strain distribution[4], stress distribution may be non-uniform. We will show that stress has a nonuniform distribution during the phase transformation and has different shapes for different loads. As an example, consider an SMA bar with diameter $d = 5$cm subjected to loading-unloading at total time of $\tau = 300sec$. The initial and ambient temperatures are $\hat{T} = T_\infty = 328K$ and air is flowing on the specimen with speed of $U_\infty = 100$ m/s that results in a forced convection coefficient of $h_\infty = 234.79W/m^2K$. Material properties are given as Material IV in Table 1. Stress distributions corresponding to different uniform strains during the loading phase is shown in Figure 11.

---

[4] The uniform strain distribution is a boundary condition considered in this special case study. The formulation of this paper is general and can be used for modeling a bar with and arbitrary strain distribution in the cross section.
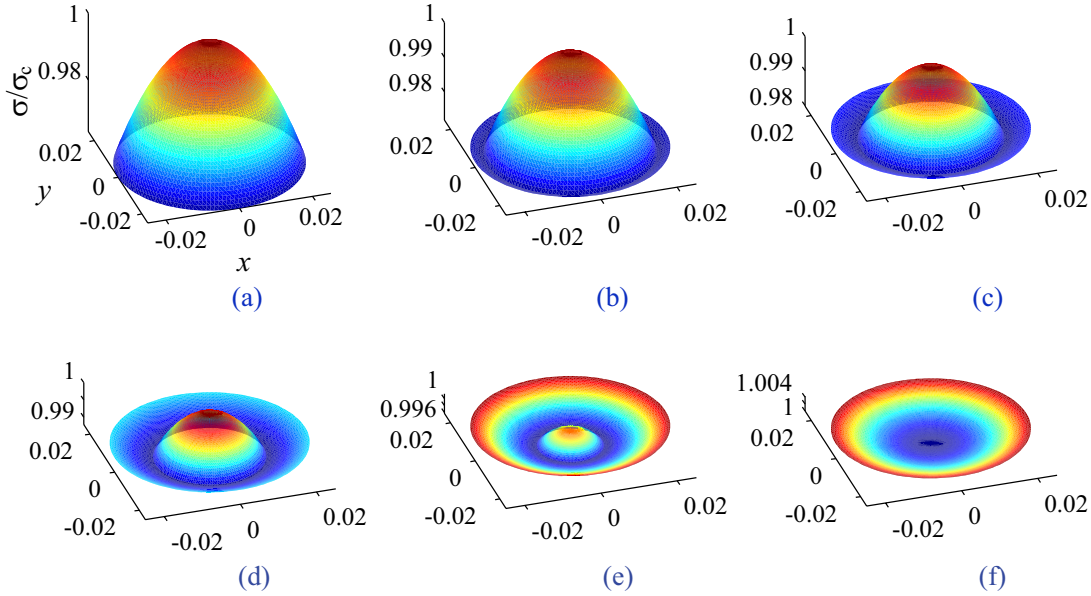
Fig. 11 Non-uniform stress distribution in the cross section of an SMA bar subjected to uniform tensile strain at (a) $\epsilon = 0.0680$, $\sigma_c = 959.0$MPa, (b) $\epsilon = 0.0768$, $\sigma_c = 994.5$MPa, (c) $\epsilon = 0.0770$, $\sigma_c = 995.6$MPa, (d) $\epsilon = 0.0773$, $\sigma_c = 996.6$MPa, (e) $\epsilon = 0.0775$, $\sigma_c = 997.5$MPa, and (f) $\epsilon = 0.085$, $\sigma_c = 1296.0$MPa.

Before the phase transformation starts, no latent heat is generated; the whole cross section has uniform stress and temperature distributions. By the start of phase transformation from austenite to martensite, latent heat is generated inside the bar. The convective heat transfer at the surface results in lower temperatures for points closer to the surface compared to the center of the bar (see Figure 10). The non-uniform temperature distribution in the cross section results in the stress distribution shown in Figure 11(a). In each of the plots in Figure 11, the stress distribution is normalized with respect to stress at the center of the bar (σ_c) for a better visualization. Stress at the center of the bar corresponding to each strain is given in Figure 11. Stress distribution in the cross section remains "convex" until the start of phase transformation completion. The phase transformation completion starts from the surface of the bar due to the lower temperature at the surface as decreasing temperature remarkably decreases the threshold of phase transformation completion in SMAs. Formation of martensite at the surface results in a decrease in stress with a sharper slope compared to the material at the inner region. The "convex" stress surface starts to invert from the outer radius as shown in Figure 11(b). By increase of load, the "convex" stress surface is inverted to a "concave" surface as shown in Figures 11(b) to 11(f). When the whole cross section is fully transformed to martensite stress distribution has the "concave" shape shown in Figure 11(f). As it is seen in Figures 11(a) to 11(f), the stress distribution nonuniformity (deviation of the normalized stress distribution surface from unity) decreases with the increase of strain and completion of phase transformation. It is worth mentioning that the strain corresponding to each stress distribution in Figure 11 is uniform.

6.5 SMA bars operating in water

The wide variety of applications of SMAs in recent years necessitates the analysis of SMA devices operating in various environments. It is now known that large scaled SMA bars and wires can be used as efficient elements for improving the seismic performance of bridges (DesRoches et al., 2010; Padgett et al., 2010; DesRoches and Delemont, 2002). The SMA tendons in bridges may operate in water and hence it is necessary to have a precise analysis of the response of these wires and bars subjected to water flow. As a case study, an SMA bar with geometric and material properties given in §6.3 is considered. It is assumed that the SMA bar

is operating as a tendon in a bridge in the water flow. The average water velocity in rivers varies from $0.1m/s$ to $3m/s$. Considering the flow velocity of $0.5m/s$ and the temperature of $T = 27°$ for the water, the forced convection coefficient is calculated using (51) and is $h_\infty = 2529.3W/m^2K$. A loading-unloading cycle in $\tau = 10sec$ is considered. The temperature distribution in the cross section at the end of loading and unloading phases is shown in Figure 12(a). As it is seen, the excessive cooling of water at the surface causes a remarkable temperature gradient in the cross section at the end of loading phase. It is obvious that ignoring this temperature distribution in the cross section is not justified in the present case study. As it is shown in this figure at the end of unloading phase the outer parts of the cross section are in a temperature below the initial temperature while the inner core has a temperature slightly above the initial temperature. This phenomenon was previously explained in Figures 6-9. The normalized stress distribution for various strain values during the loading phase are shown in Figure 12(b). As it is shown in this figure, the convex to concave transformation of the stress distribution shape is seen in this case study as well (this phenomenon was explained in detail in §6.4). Comparing the results of Figures 12(b) and 11 reveals that while the stress difference in the cross section of a bar cooling in flowing air is 4%, it increases to 14% in the present case study (SMA bar operating in water).
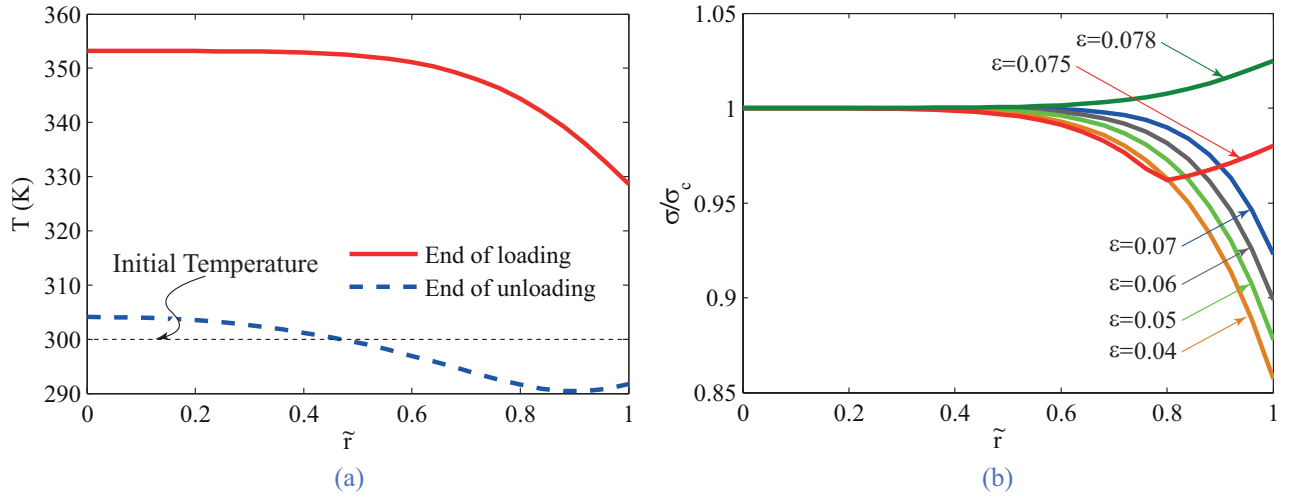

Fig. 12 (a) Temperature distribution in the cross section, and (b) stress distribution in the loading phase for an SMA bar with $d = 5$cm operating in water. The stress at the center point for strain values $\epsilon = 0.04$, 0.05, 0.06, 0.07, 0.075, and 0.078 are $\sigma_c = 582.2$, 631.6, 676.2, 722.5, 864.1, and 958.2MPa, respectively.

6.6 Size, boundary condition, and loading rate effects on the temperature and stress gradients

As it was shown in the previous sections, the gradients of temperature and stress in the cross section are strongly affected by the ambient condition, diameter of the bar, and the loading-unloading rate. In this section we study the effect of these parameters on the maximum temperature and stress gradients in the cross section of SMA bars and wires subjected to uniaxial loading. For sake of brevity, we consider only the loading phase. The initial and ambient temperatures are assumed to be $T_0 = T_\infty = 300K$ for all the case studies in this section. In each case, for studying the non-uniformity in stress and temperature distributions in the cross section, the difference between the value of these parameters at the center and surface of the bar is nondimensionalized by dividing by the value of the corresponding parameter at the surface. The maximum temperature and stress gradients versus the convection coefficient for four various loading rates are shown in Figure 13. A bar with $d = 5cm$ and material properties similar to the previous case study is considered and the range of convection coefficient is chosen to cover the free and forced convection of air, and water flow on the bar (see the case studies in §6.3 and 6.5). As it is shown in this figure for all the loading rates both the

temperature and stress gradients increase for larger convection coefficients. However, for the slow loading rate $\tau = 300sec$, the increase of gradient is suppressed for convection coefficients larger than $h_\infty \simeq 1000W/m^2K$, since the material has enough time to exchange heat with the ambient. It is worth noting that for the slow loading rate $\tau = 300$ sec the trend of the gradient change is different from the other (fast) loading rates. We will study the effect of changing the loading rate on the gradients in the following case study and will find the critical time corresponding to this change of trend for some sample ambient conditions. It is shown in Figure 13 that the temperature and stress gradients in the cross section are more excessive for larger convection coefficients for all the loading rates.
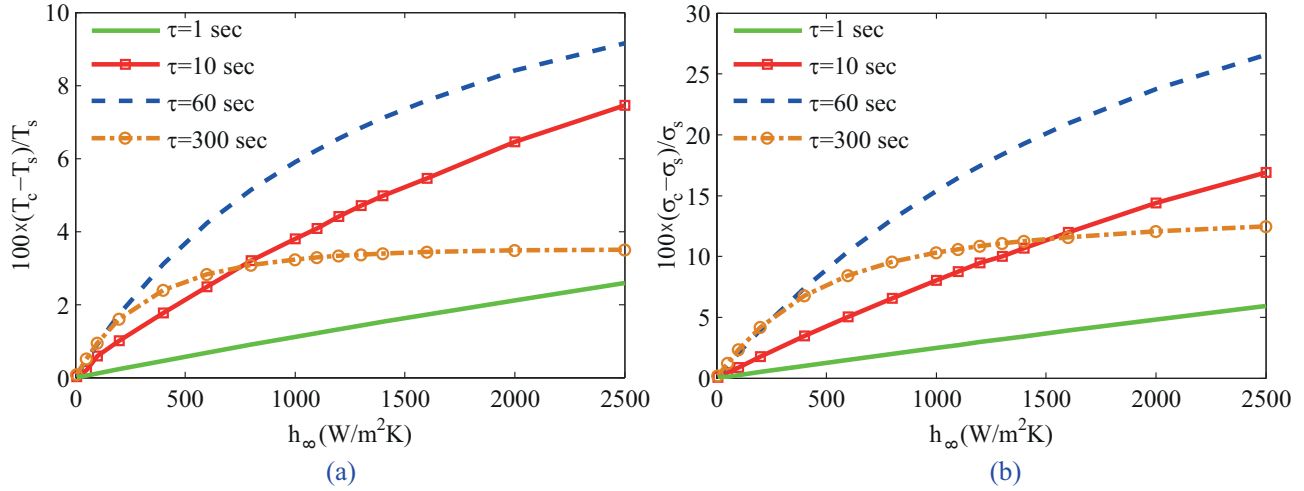

Fig. 13 (a) The maximum temperature gradient, and (b) the maximum stress gradient versus the convection coefficient for four different loading rates. The subscripts s and c denote the value measured at the surface and center of the bar, respectively. The diameter of the bar is $d = 5cm$.

The effect of changing the loading rate on the maximum temperature and stress nonuniformity in the cross section for three different convection coefficients is shown in Figure 14. The results are presented for the total loading-unloading times $1 \leq \tau \leq 3600sec$. As it is shown, larger convection coefficients lead to more nonuniformity for both the stress and temperature distributions. Also, it is shown that for all the convection coefficients the temperature and stress gradients are negligible for very fast and very slow loading rates, and peaks at an intermediate loading rate ($\tau = 140sec$ for $h_\infty = 134W/m^2K$, $\tau = 100sec$ for $h_\infty = 234W/m^2K$, and $\tau = 30sec$ for $h_\infty = 2529W/m^2K$). This is expected because for very fast loadings the material at the surface does not have enough time to exchange the latent heat with the ambient and the temperature and stress distributions are almost uniform. For very slow loadings, the latent heat in the whole cross section has enough time to be exchanged with the ambient and the temperature and stress distributions are almost uniform in the cross section. For an intermediate loading rate the temperature and stress distribution nonuniformity is maximum. Also it is worth mentioning that the loading rate corresponding to the maximum nonuniformity decreases by increasing the convection coefficient.

The size effect on the temperature and stress nonuniformity is studied for three different ambient conditions in Figure 15 (the total loading-unloading time is $\tau = 10sec$). As explained in §5, the convection coefficient depends on the bar diameter and for obtaining the results presented in Figure 15 the appropriate convection coefficient for each diameter and ambient condition is calculated using the formulation of §5. As it is shown in Figure 15, in the case of water flow the temperature and stress nonuniformities are more pronounced compared to those of the air flow ambient condition. For the forced convection by air the temperature and stress gradients increase for larger diameters. However, in the case of water flow, the gradients have a peak at $d \simeq 25mm$.

The results presented in Figures 13-15 clearly describe the complicated effect of size, ambient condition, and loading rate on the coupled thermo-mechanical response of SMA bars. These figures can be used by a designer to decide whether a coupled thermo-mechanical formulation with considering the heat flux in the cross section is necessary or using simpler lumped models is enough. It is worth mentioning that although for
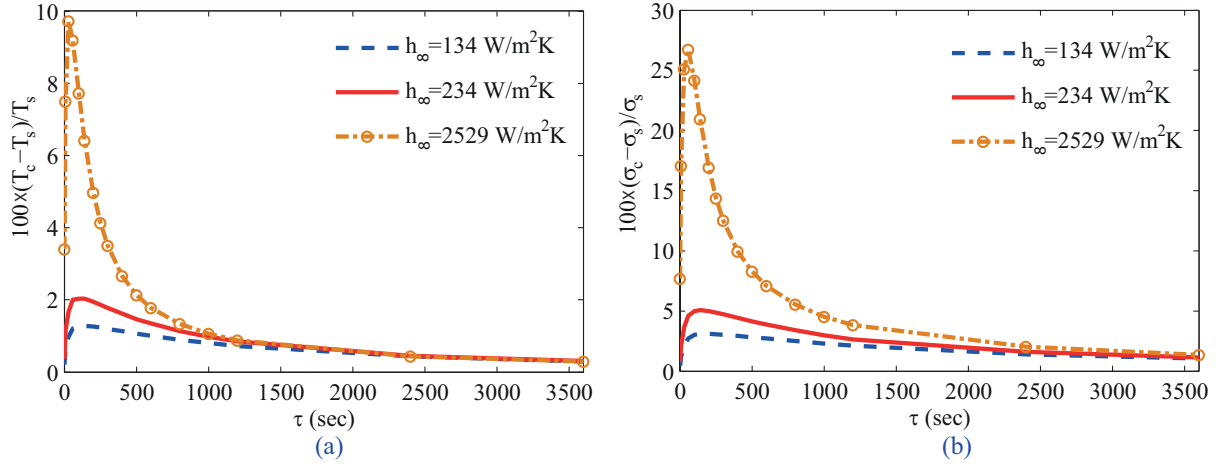
Fig. 14 (a) The maximum temperature gradient and (b) the maximum stress gradient versus the loading rate for three various convection coefficients. The subscripts s and c represent the value measured at the surface and center of bar respectively. The diameter of bar is d=5cm.
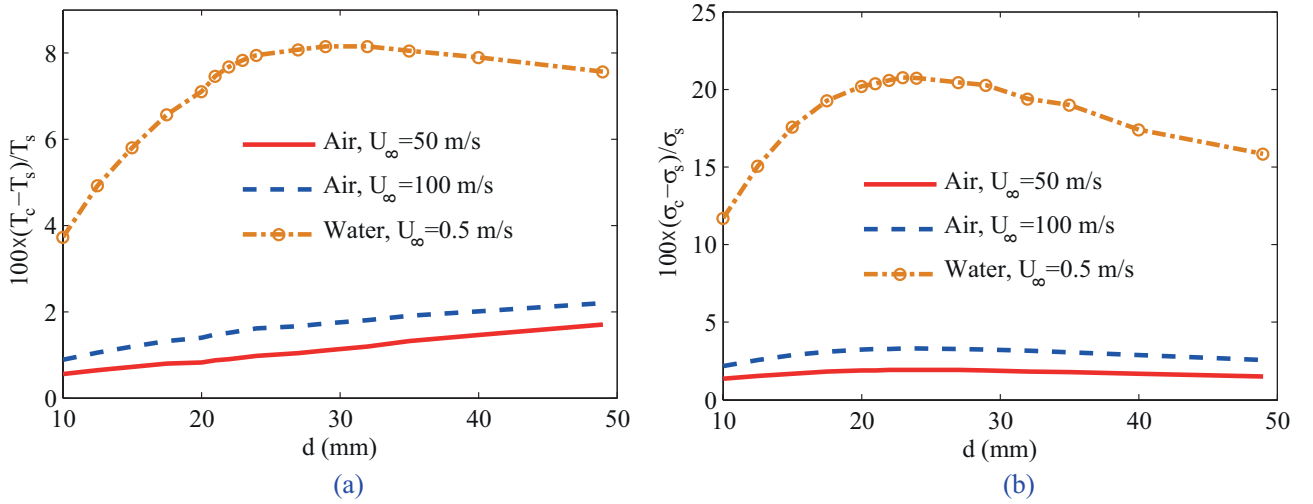

Fig. 15 (a) The maximum temperature gradient and (b) the maximum stress gradient versus the bar diameter for three various ambient conditions. The subscripts s and c represent the value measured at the surface and center of bar, respectively. The total loadig-unloading time is τ =10 sec.

the uniaxial loading of bars and wires the simpler models assuming lumped temperature in the cross section can be used with an error, there are numerous cases for which the present formulation is the only analysis option. An example is torsion of circular SMA bars for which shear stress has a complicated nonuniform distribution in the cross section (Mirzaeifar *et al.*, 2010a). It would be incorrect to consider a lumped temperature in the cross section for torsion problems. Considering the effect of phase transformation latent heat in torsion of SMA bars is the subject of a future communication. We have been able to show that ignoring the heat flux and the temperature nonuniformity in the cross section of SMA bars subjected to torsion leads to inaccurate results. It is also worth nothing that all the numerical simulations presented in this paper are performed on a 2 GHz CPU with 2 GB RAM. Since the presented explicit finite difference formulation needs a variable minimum time increment for guarantying numerical stability for various dimensions and material properties (Özişik, 1994), the computational time varies for different case studies. However, by considering an average of 30 nodes (for smaller diameters fewer nodes are used) in the cross section and using the material

properties in Table 1, the most time consuming case studies (examples with large number of nodes in the cross section and large loading-unloading times) are all completed in less than 20 minutes.

7 Conclusions

In this paper, a coupled thermo-mechanical framework considering the effect of generated (absorbed) latent heat during forward (reverse) phase transformation is presented for shape memory alloys. The governing equations are discretized for SMA bars and wires with circular cross sections by considering the non-uniform temperature distribution in the cross section. Appropriate convective boundary conditions are used for still and flowing air and also flowing water on slender and thick cylinders. The present formulation is capable of simulating the uniaxial thermo-mechanical response of SMA bars and wires by taking into account the effect of phase transformation-induced latent heat in various ambient conditions. The results of some experiments are used for evaluating the accuracy of the present formulation in modeling the rate dependency and temperature changes in uniaxial loading of SMA wires and bars. Several numerical examples are presented for studying the interaction between thermo-mechanical coupling, loading rate, ambient conditions, and size of the specimen. It is shown that a loading being quasi static strongly depends on external conditions, e.g. the size and ambient conditions. Temperature distribution in the cross section is also studied and it is shown that the loading rate, ambient conditions, and size of the specimen affect the temperature distribution.

The method of this paper can be used for an accurate simulation of the material response of SMA devices in the presence of rate-dependency, size, and ambient condition effects. The present method can be exploited to analyze SMA bars with various cross sections. Our three-dimensional coupled-thermo-mechanical formulation can be used for studying other loadings, e.g. torsion, bending, and combined loadings. Also, the constitutive equations used in this work can be modified to take into account the accumulated fatigue strains. These will be the subject of future communications.

References

Airoldi G, Riva G, Rivolta B, Vanelli M. DSC calibration in the study of shape memory alloys. *Journal of thermal analysis*. 1994; 42(4): 781-791.

Arpaci VS. Conduction heat transfer, Addison-Wesle: Reading, Massachusets, 1966.

Auricchio F, Fugazza D, Desroches R. Rate-dependent thermo-mechanical modelling of superelastic shape-memory alloys for seismic applications. *Journal of Intelligent Material Systems and Structures*. 2008; 19: 47-61.

Bernardini D, Vestroni F. Non-isothermal oscillations of pseudoelastic devices. *International Journal of Non-Linear Mechanics*. 2003; 38: 1297-1313.

Birman V. Review of mechanics of shape memory alloy structures. *Applied Mechanics Reviews*. 1997; 50(11) 629-645.

Boyd JG, Lagoudas DC. A thermodynamic constitutive model for the shape memory alloy materials. Part I. The monolithic shape memory alloy. *International Journal of Plasticity*. 1996; 12: 805-842.

Cebeci, T. Laminar free convective heat transfer from the outer surface of a vertical slender circular cylinder. *Proc. 5th Int. Heat Transfer Conference*. 1974. vol. 3, PaperNC1.4, Tokyo, 15?19.

Chang BC, Shaw JA, Iadicola MA. Thermodynamics of shape memory alloy wire: modeling, experiments, and application. *Continuum Mechanics and Thermodynamics*. 2006; 18: 83-118.

Chen YC, Lagoudas DC. Impact induced phase transformation in shape memory alloys. *Journal of the Mechanics and Physics of Solids*. 2000; 48(2): 275-300.

DesRoches R, Delemont M. Seismic retrofit of simply supported bridges using shape memory alloys. *Engineering Structures*. 2002; 24(3): 325-332.

DesRoches R, McCormick J, Delemont M. Cyclic properties of superelastic shape memory alloy wires and bars. *Journal of Structural Engineering*. 2004; 130(1): 38-46.

DesRoches R, Taftali B, Ellingwood BR. Seismic performance assessment of steel frames with shape memory alloy connections. Part I analysis and seismic demands. *Journal of Earthquake Engineering*. 2010; 14(4): 471-486.

Fand RM. Heat transfer by forced convection from a cylinder to water in crossflow. *International Journal of Heat and Mass Transfer*.1965; 8(7): 995-1010.

Forsythe GE, Malcolm MA, Moler CB. Computer methods for mathematical computations. 1976. Prentice-Hall.

Gall K, Sehitoglu H, Chumlyakov YI and Kireeva IV. Tension-compression asymmetry of the stress-strain response in aged single crystal and polycrystalline NiTi. *Acta Materialia*. 1999; 47: 1203-17.

Goo BC, LexcellentC. Micromechanics-based modeling of two-way shape memory effect of a single crystalline shape memory alloy. *Acta Metallurgica et Materialia*. 1997; 45(2): 727-737.

Gao X, Huang M, Brinson LC. A multivariant micromechanical model for SMAs. Part 1: Crystallographic issues for single crystal model. *International Journal of Plasticity*. 2000; 16(10?11): 1345-1369.

He XM. Rong LJ. DSC analysis of reverse martensitic transformation in deformed Ti-Ni-Nb shape memory alloy. *Scripta Materialia*. 2004; 51(1): 7-11.

Hilpert R. Wärmeabgabe yon geheizten drähten und rohern im lufstrom. *Forsch. Geb. Ingenieurw.* 1933; 4: 215-224.

Holman, JP. Heat transfer. 7th ed. McGraw-Hill: New York. 1990.

Iadicola MA, Shaw JA. Rate and thermal sensitivities of unstable transformation behavior in a shape memory alloy. *International Journal of Plasticity*. 2004; 20: 577-605.

Knudsen JG, Katz DL. Fluid Dynamics and Heat Transfer. McGraw-Hill: New York. 1958.

Lagoudas DC, Bo Z, Qidwai MA. A unifed thermodynamic constitutive model for SMA and finite element analysis of active metal matrix composite. *Mechanics of Composite Materials and Structures*. 1996; 3: 153-179.

Lagoudas DC, Ravi-Chandar K, Sarh K, Popov P. Dynamic loading of polycrystalline shape memory alloy rods. *Mechanics of Materials*. 2003; 35: 689-716.

Lagoudas DC, Entchev PB. Modeling of transformation-induced plasticity and its effect on the behavior of porous shape memory alloys. Part I: constitutive model for fully dense SMAs. *Mechanics of Materials*. 2004; 36(9): 865-892.

Lagoudas DC, Entchev PB, Popov P, Patoor E, Brinson LC, Gao X. Shape memory alloys, Part II: Modeling of polycrystals. *Mechanics of Materials*. 2006; 38: 430-462.

Lagoudas, DC, (Editor). Shape memory alloys: modeling and engineering applications. Springer: New York. 2008.

Liang C, Rogers CA. The multi-dimensional constitutive relations of shape memory alloys. *Journal of Engineering Mathematics*. 1992; 26: 429-443.

Liu N, Huang WM. DSC study on temperature memory effect of NiTi shape memory alloy. *Transactions of Nonferrous Metals Society of China*. 2006; 16: s37-s41.

McCormick J, Tyber J, DesRoches R, Gall K, Maier HJ. Structural engineering with NiTi. II: mechanical behavior and scaling. *Journal of Engineering Mechanics*. 2007; 133(9): 1019-1029.

Messner C, Werner EA. Temperature distribution due to localised martensitic transformation in SMA tensile test specimens. Computational Materials Science. 2003; 26: 95-101.

Mirzaeifar R, Shakeri M, Sadighi M. Nonlinear finite element formulation for analyzing shape memory alloy cylindrical panels. *Smart Materials and Structures*. 2009; 18(3). 035002.

Mirzaeifar R, DesRoches R, Yavari A. Exact solutions for pure torsion of shape memory alloy circular bars. *Mechanics of Materials*. 2010; 42(8): 797-806.

Mirzaeifar R, Shakeri M, DesRoches R, Yavari A. A semi-analytic analysis of shape memory alloy thick-walled cylinders under internal pressure. *Archive of Applied Mechanics*. 2010. DOI: 10.1007/s00419-010-0468-x.

Mirzaeifar R, DesRoches R, Yavari A. A combined analytical, numerical, and experimental study of shape-memory-alloy helical springs. *International Journal of Solids and Structures*. 2011. 48(3-4): 611-624.

Özişik MN. Finite difference methods in heat transfer. CRC-Press: Boca Raton, Florida. 1994.

Padgett JE, DesRoches R, Ehlinger R. Experimental response modification of a four-span bridge retrofit with shape memory alloys. *Structural Control and Health Monitoring*. 2010; 17(6): 694-708.

Paradis A, Terriault P, Brailovski V. Modeling of residual strain accumulation of NiTi shape memory alloys under uniaxial cyclic loading. *Computational Materials Science*. 2009; 47: 373-383.

Patoor E, Lagoudas DC, Entchev PB, Brinson LC, Gao X. Shape memory alloys, Part I: General properties and modeling of single crystals. *Mechanics of Materials*. 2006; 38: 391-429.

Popiel CO. Free convection heat transfer from vertical slender cylinders: a review. *Heat Transfer Engineering*, 2008; 29(6): 521-536.

Qidwai MA, Lagoudas DC. On thermomechanics and transformation surfaces of polycrystalline NiTi shape memory alloy material. *International Journal of Plasticity*. 2000; 16: 1309-1343.

Qidwai MA, Lagoudas DC. Numerical implementation of a shape memory alloy thermomechanical constitutive model using return mapping algorithms. *International Journal for Numerical Methods in Engineering*.

2000; 47: 1123-68.

Rajagopal KR, Srinivasa AR, Mechanics of the inelastic behavior of materials. part I: Theoretical underpinnings. *International Journal of Plasticity.* 1998; 14(10-11): 945-967.

Saint-Sulpice L, Chirani SA, Calloch S. A 3D super-elastic model for shape memory alloys taking into account progressive strain under cyclic loadings. *Mechanics of Materials.* 2009; 41: 12-26.

Simo JC, Hughes TJR, Computational inelasticity, Vol. 7 of interdisciplinary applied mathematics, Springer-Verlag, New York, 1998.

Tanaka K. A thermomechanical sketch of shape memory effect: one-dimensional tensile behaviour. *Res Mechanica.* 1986; 18: 251-63.

Tanaka K, Kobayashi S, Sato Y. Thermomechanics of transformation pseudoelasticity and shape memory effect in alloys. *International Journal of Plasticity.* 1986; 2: 59-72.

Tanaka K, Nishimura F, Hayashi T, Tobushi H, Lexcellent C. Phenomenological analysis on subloops and cyclic behavior in shape memory alloys under mechanical and/or thermal loads. *Mechanics of Materials.* 1995; 19: 281-292.

Tyber J, McCormick J, Gall K, DesRoches R, Maier H, Maksoud AEA. Structural Engineering with NiTi. I: Basic Materials Characterization. *Journal of Engineering Mechanics.* 2007; 133(9): 1009-1018.

Vitiello A, Giorleo G, Morace RE. Analysis of thermomechanical behaviour of Nitinol wires with high strain rates. *Smart Materials and Structures.* 2005; 14: 215-221.